

Review

# Advances in Hybrid Composites for Photocatalytic Applications: A Review

Stefania Porcu <sup>1</sup>, Francesco Secci <sup>2</sup> and Pier Carlo Ricci <sup>1,\*</sup><sup>1</sup> Department of Physics, University of Cagliari, S.P. No. 8 Km 0.700, 09042 Monserrato, Italy<sup>2</sup> Department of Chemical and Geological Science, University of Cagliari, S.P. No. 8 Km 0.700, 09042 Monserrato, Italy

\* Correspondence: carlo.ricci@dsf.unica.it; Tel.: +39-070675-4821

**Abstract:** Heterogeneous photocatalysts have garnered extensive attention as a sustainable way for environmental remediation and energy storage process. Water splitting, solar energy conversion, and pollutant degradation are examples of nowadays applications where semiconductor-based photocatalysts represent a potentially disruptive technology. The exploitation of solar radiation for photocatalysis could generate a strong impact by decreasing the energy demand and simultaneously mitigating the impact of anthropogenic pollutants. However, most of the actual photocatalysts work only on energy radiation in the Near-UV region (<400 nm), and the studies and development of new photocatalysts with high efficiency in the visible range of the spectrum are required. In this regard, hybrid organic/inorganic photocatalysts have emerged as highly potential materials to drastically improve visible photocatalytic efficiency. In this review, we will analyze the state-of-art and the developments of hybrid photocatalysts for energy storage and energy conversion process as well as their application in pollutant degradation and water treatments.

**Keywords:** photocatalysis; semiconductor photocatalysts; hybrid systems; organic/inorganic heterostructures



**Citation:** Porcu, S.; Secci, F.; Ricci, P.C. Advances in Hybrid Composites for Photocatalytic Applications: A Review. *Molecules* **2022**, *27*, 6828. <https://doi.org/10.3390/molecules27206828>

Academic Editor: Barbara Bonelli

Received: 7 September 2022

Accepted: 9 October 2022

Published: 12 October 2022

**Publisher's Note:** MDPI stays neutral with regard to jurisdictional claims in published maps and institutional affiliations.



**Copyright:** © 2022 by the authors. Licensee MDPI, Basel, Switzerland. This article is an open access article distributed under the terms and conditions of the Creative Commons Attribution (CC BY) license (<https://creativecommons.org/licenses/by/4.0/>).

## 1. Introduction: Importance and Limits

The research and the development of new solutions that strengthen industrial and technological progress, guaranteeing sustainable impacts, is greatly boosting the effort of the scientific community. Modern household combustion devices, motor vehicles, and industrial facilities are common sources of air and water pollution. Particulate matter, nitrogen oxide, sulfur dioxide, volatile organic compounds, dioxins, and polycyclic aromatic hydrocarbons are considered pollutants that are greatly harmful to humans. Outdoor and indoor air pollution cause respiratory and other diseases and are important sources of morbidity and mortality. Policies to reduce air and water pollution represent a winning strategy for both climate and health, lowering the burden of disease attributable to air pollution, as well as contributing to the near- and long-term mitigation of climate change. An interesting review of the environmental and health impact of air pollution is reported by Manisaldis et al., [1] analyzing the sources of environmental pollution in relation to public health and environmental effects. Boosting education, training, public awareness, and public participation are some of the relevant actions indicated in the Paris Agreement of 2015, issued by the UNFCCC (United Nations Climate Change Committee) for maximizing the opportunities to achieve a sustainable impact by the anthropogenic actions, mitigating the climate change and environmental pollution [2]. The raising of environmental technologies can greatly support political/social actions and virtuous daily behaviors. Some examples can be sketched, such as the use of renewable energy obtained by sunlight, wind, rain, waves, and geothermal heat, the definition of smart mass transportation, and highly efficient electric vehicles. However, several factors should be considered in the definition and the use of “green” technologies, starting from the materials and their complete cycle of life,

the efficiency, the environmental impact, and the up-grading possibilities. On these bases, photocatalysis is strongly indicated as a promising technology having a fundamental role in applications such as fuel cells, solar conversion, healthy treatments, and environmental radiation (Figure 1). If water splitting has been intensively studied as a possible approach to achieve the effective conversion of solar into chemical energy, photocatalysis is also utilized to decrease the number of organic compounds in the air, water, or soil, representing a high environmental risk for health.

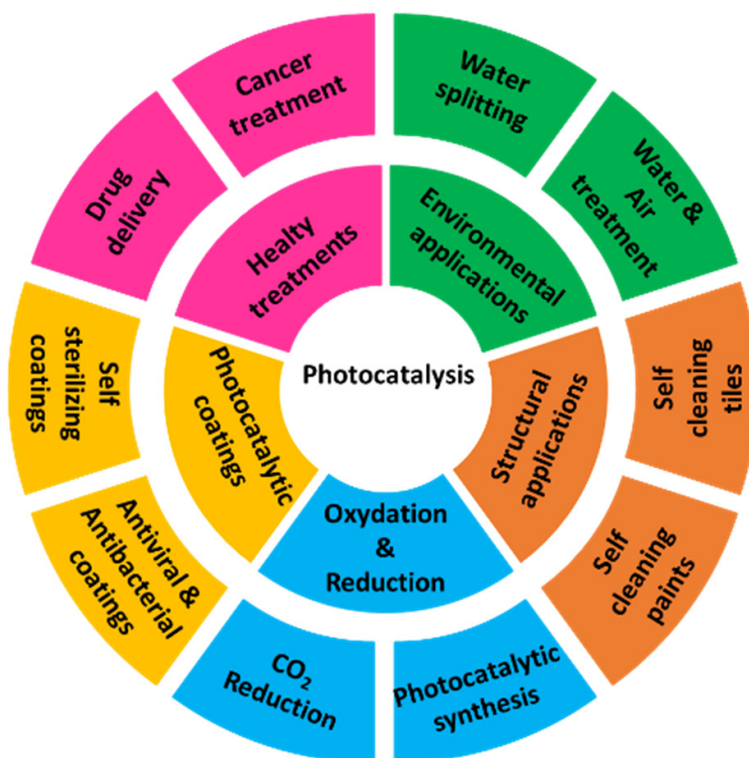


**Figure 1.** Application fields of photocatalysis.

Photocatalysis has been applied to degrade several types of organic waste, such as dyes [3,4], phenolic compounds [5,6], organohalides, and petroleum hydrocarbons [7], but also for the removal of heavy metals such as Chromium, Lead, or Mercury among the others [8,9]. The photocatalytic techniques have been applied even to the degradation of pharmaceutical compounds (PC) that represent a new and emerging source of waste in water and soils [10]. Antibiotics and their by-products have high toxicity, good stability, and great potential to interfere with the environment and ecological environment. Many antibiotics are discharged into the water environment through sewage and animal feces, causing severe water and soil environmental problems [11]. Anti-inflammatory drugs have a high polarity and strong hydrophilicity, but the absorption coefficient in the soil is low, so they are easy to survive underground, surface, and even drinking water resources, causing great pollution to water resources.

The term “photocatalysis” and the base of the effect are already known from the end of the 19th century when Giacomo Ciamician defined the term photocatalysis for the first time. Successively, it is worth mentioning that the first results on photocatalytic water splitting using a  $\text{TiO}_2$  electrode were reported by Fujishima and Honda in 1972 [12]. After that, the research on this field strongly increased, and in the last 20 years, the number of publications on “photocatalysis” has constantly grown up to 8737 publications in 2021 (Figure 2).

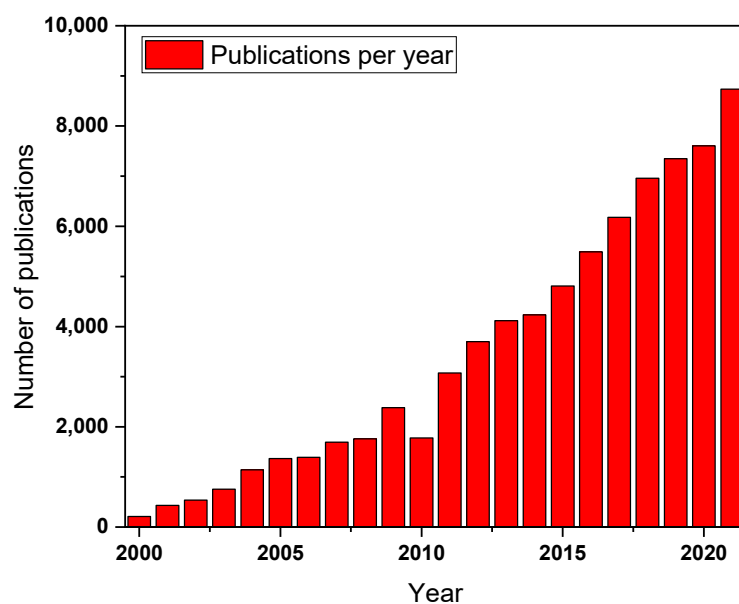


**Figure 2.** Representative scheme of the publication rate of papers regarding photocatalysis.

Moreover, the “old” knowledge, the research in this field, and, mostly, the development of new materials with higher efficiency is a mandatory step to overcome the actual technical limits of the processes. Most photocatalysts can utilize the sizeable visible component of the solar spectrum very partially, working on higher energy photons (UV range) that count for only 5% of the solar emission.

Recently different strategies and materials have been utilized to overcome this issue: lowering the band gap of the materials, new energetic levels by doping process, and heterostructures with increased charge separation are just a few examples that we better discuss in the review. On the other hand, the achievement, or at least the improvement in this direction, has a strong potential impact on our daily life and, mostly, on the environmental aspect for a long-time vision of sustainable progress.

Sunlight is a free, perpetual, and clean energy source. If we consider that photocatalysis is a light-induced chemical pathway able to convert organic material into energy, the benefits of this process appear immediate. However, even if the energy produced from the sun is renewable and gives us a plethora of advantages, the materials needed to convert it into practical use should be carefully chosen to guarantee an environmentally friendly process. They should be free from potential impact connected to the extraction of the raw materials and precursors, the use of solvents in the synthesis procedure, and the energy required in the whole life cycle of the photocatalysts should be carefully checked [13,14].

Among the wide choice in terms of possible materials, photocatalysts can be classified into two main categories: semiconductors (organic or inorganic) and metal nanoparticles. Transition metals such as gold, copper, and silver are characterized by localized surface plasmon resonance (LSPR), while semiconducting materials such as  $\text{TiO}_2$ ,  $\text{ZnO}$ ,  $\text{SnO}_2$ ,  $\text{MoS}_2$ ,  $\text{Bi}_2\text{MoO}_6$  [15–20] assure complete mineralization, no waste disposal problem, low cost and necessity of mild temperature and pressure conditions. Organic materials show mechanical and chemical properties that radically differentiate them from inorganic ones. The absence of metals, the high possibilities to tune the synthesis technique, and the high varieties of optical and structural character of the organic photocatalyst, justify the high interest in this class of materials. Within the organic chemistry panorama, polymers can guarantee very high versatility in terms of structural and optical response with high potential in several applications, but their efficiency is generally hampered by the low thermal and short-time structural stability of the compounds. As already mentioned, different thousands of articles and studies are constantly published, and the interest of the scientific community is strongly active in this field. On these bases, it is important to summarize time by

time, the state-of-the-art progress in the design of a variety of semiconductor composite photocatalysts for energy and environmental applications. In recent years different review articles were focalized on photocatalysis, from base properties [21–24] to materials [25–28] and to applications.

Inside these very broad categories, several aspects have been considered. If Humayun et al. [29] pointed out the synthesis procedures of composite photocatalysts and the use of microwave is underlined, other works focalize on a specific class of materials: MOF [25], metal halide perovskite [26], graphene [28], and carbon nitride [30].

The use of the photocatalytic process in water treatments [31], for the removal of Volatile Organic compounds (VOC) [32], and the abatement of plastics [33] are just a few recent examples, such as its use for the degradation of persistent herbicides [34] or, more in general, for the development of sustainable agriculture [35].

In this review, we will briefly analyze the state art in inorganic and organic semiconductor photocatalysts, mainly focalizing our discussion on the method to obtain efficient processes using visible light. We will underline the efforts of the scientific community to build efficient heterostructures, and we will analyze the new solutions based on hybrid systems, organic-inorganic, that efficiently work with a relative portion of the solar spectrum.

## 2. Basic Principles of Photocatalysis

A Photocatalytic process occurs when the light interacts with the surface of semiconductor materials, the so-called photocatalysts, allowing the photo redox process. During this process, there must be at least two simultaneous reactions occurring, oxidation from photogenerated holes and reduction from photogenerated electrons (Figure 3) [36–38].

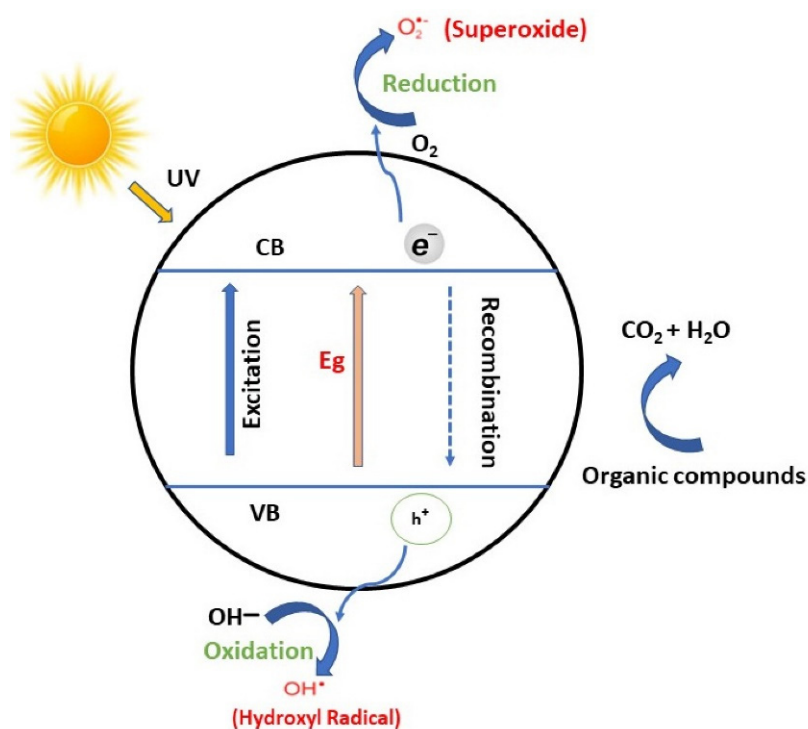


**Figure 3.** Basic scheme of semiconductor-mediated photocatalytic process [38].

The process can be divided into four fundamental steps: (I) light absorption to generate electron-hole pairs; (II) separation of excited charges; (III) transfer of electrons and holes to the surface of photocatalysts; (IV) utilization of charges on the surface for redox reactions [39]. The holes left in the valence band have high oxidizing power and, reacting with water, generate hydroxyl radicals responsible for pollutant degradation. The electrons in the conduction band, via reaction with dissolved oxygen species, form superoxide ions that promote the reduction process [36,40].

In the oxidation process, the positive holes in the valence band allow oxidizing of the water at the surface of the catalyst, forming hydroxyl radicals ( $\text{OH}\cdot$ ) with a high oxidative decomposing power. These hydroxyl radicals react with the organic pollutant that, at the end of the process, is decomposed into carbon dioxide and water. As well, the organic compounds could react directly with the positive holes created in the valence band, activating an oxidative decomposition.

The reduction process of the oxygen contained in the air is an alternative reaction to hydrogen generation since oxygen is an easily reducible substance. The electrons in the conduction band, reacting with the dissolved oxygen species, form superoxide anions that, after being attached to the intermediate products obtained from the oxidative reaction, form peroxide or hydrogen peroxide and then water as the final product.

The photocatalytic activity of a material depends on several parameters: morphology, size, surface area, reaction temperature, pH, light intensity, amount of catalyst, and concentration of wastewater dependent. The structure of the catalyst plays a fundamental role in the photocatalytic activity: the stability of the catalyst, the position of the conduction band, the degree of hydroxylation and the absorption power, and the size of the particles. In general, the smaller the size of the catalyst nanoparticles, the higher the photocatalytic activity. Cerruto et al. systematically correlated the photocatalytic activity to the average sizes and size distributions of  $\text{TiO}_2$  nanocrystals [41], while more recently, the study was extended to the hydrogen produced by Al-doped  $\text{SrTiO}_3$  photocatalysts [42] to the visible photocatalytic activity in  $\beta\text{-Bi}_2\text{O}_3$  [42,43], and the reduction of  $\text{CO}_2$  in  $\text{Cu}/\text{Cu}_2\text{O}$  nanocrystals [44]. The surface properties significantly influence the efficiency of the catalyst because, during the photocatalytic process, oxidation and reduction reactions take place on the surface of the catalyst [45,46].

On this topic, He et al. found that the differences in the photocatalytic activity of different shaped samples of  $\text{ZnO}$  are not caused by the changes in specific surface area, oxygen defects, or particle size, but it was attributed to the pore size. The pore size determines the adsorption efficiency of organic pollutants and dissolved oxygen, and good adsorption performance is the main prerequisite for efficient catalytic degradation [47].

An increase in the temperature during the photocatalytic process induces a decrease in photocatalytic activity. Since the activation is due only to photonic interaction, the photocatalytic systems can operate at room temperature [48]. Even pH plays a key role in photocatalytic reactions because it is responsible for the surface charge properties of the photocatalyst. This could be explained in terms of electrostatic interactions between charged particles and contaminants, influencing the absorption and, consequently, the surface properties [49–51]. From multiple studies, it was also evaluated that the degradation rate is directly proportional to the catalyst concentration. An increase in the amount of the catalyst during the photocatalytic process is reflected in the highest number of active sites formed on the semiconductor surface and in an increasing number of  $\text{OH}\cdot$  and  $\text{O}_2^{\cdot-}$  radicals [52].

Another fundamental factor in estimating the degradation rate during a photocatalytic process is the type of pollutant and its concentration. Having different pollutants and different irradiation times to complete mineralization is needed [36,48,52,53].

### 3. Semiconductor Photocatalysts

Photocatalysts are defined as a class of materials that absorb light and can convert it into electrical charges driving the reduction and/or oxidation of species at the catalyst surface. During the last three decades, great attention has been focused on semiconductor metal oxides, selenides, and sulfides as photocatalysts thanks to their bandgap energy between 1.1 and 3.8 eV and their redox potential (Figure 4) [40]. The species with a higher reduction potential have a higher tendency to acquire electrons, while the species with a higher oxidation potential tend to lose them and to be oxidized.

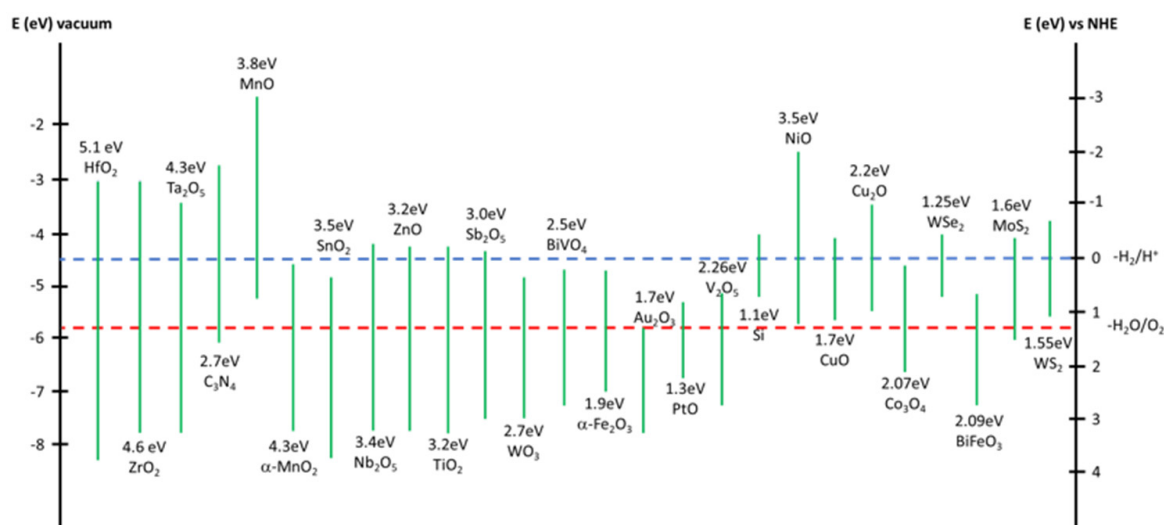
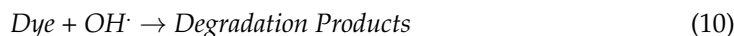
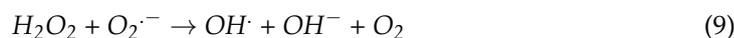
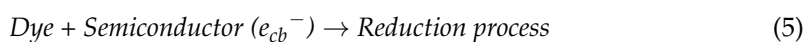


**Figure 4.** Semiconductor's band-gaps and redox potentials.

Metal oxides are largely considered the most efficient and widely applied materials, while metal selenides and sulfides are poorly considered for their toxicity and poor stability [46,54]. In general, the photocatalytic mechanism in semiconductors can be sketched with the below-mentioned Equations (1)–(10).



Currently, the most attractive photocatalytic materials are n-type semiconductors such as  $\text{TiO}_2$ ,  $\text{WO}_3$ , and  $\text{Fe}_2\text{O}_3$ , because of their high chemical stability and a conduction band edge with a potential level that is negative enough to allow the proton reduction without additional electric bias [55–58].

As already stated, the first studies of  $\text{TiO}_2$  as a photocatalyst is date back to 1972, and then in 1977, Bard applied it for the first time to purify water from  $\text{CN}^-$  ions [59].

To date,  $\text{TiO}_2$  is considered an n-type semiconductor with several advantages (high photoactivity, strong oxidizing capability, cost-effectiveness, low toxicity, and high stability) and represents one of the most widely studied and applied semiconductor photocatalysts. On the other hand, it still suffers, such as all the inorganic semiconductors, of high recombination rate and negligible light harvesting in the visible range.

In order to overcome the bottlenecks above, the research has been focused on improvements in solar spectral absorption and decreasing the recombination rate of these photocatalysts (Figure 5).

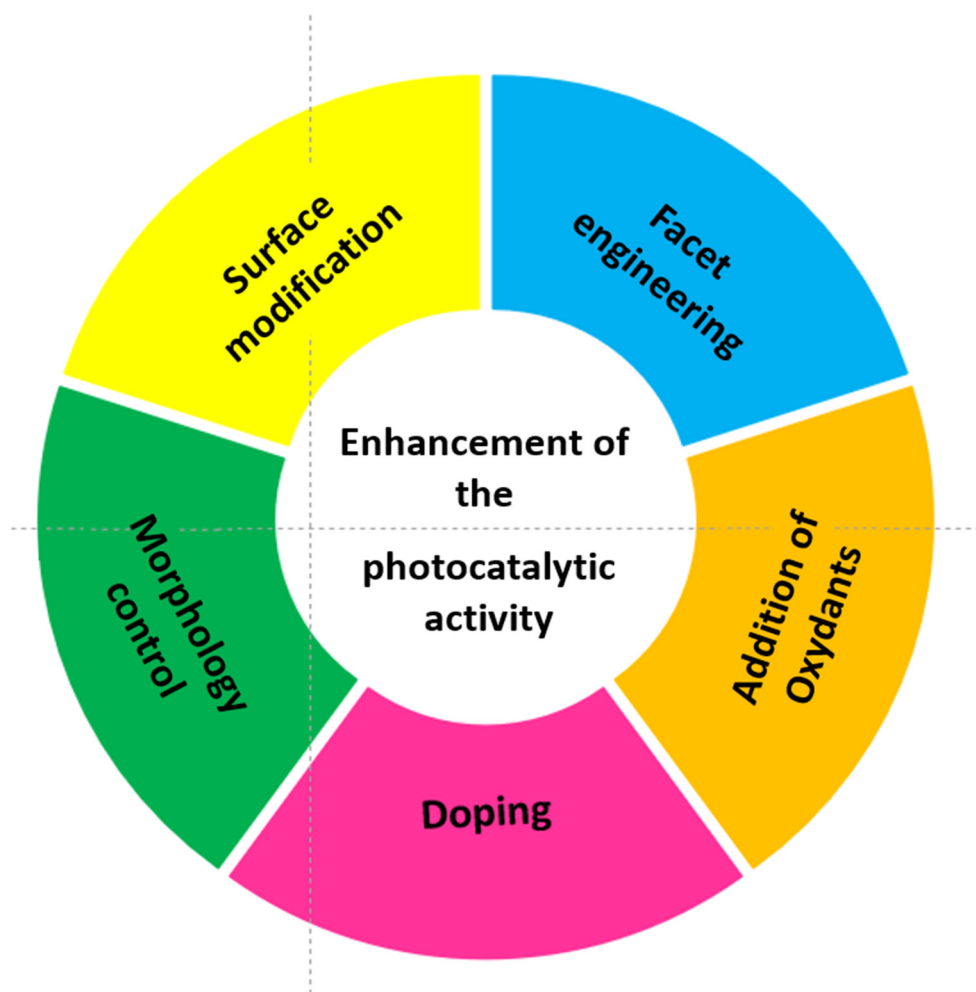


**Figure 5.** Strategies to enhance the photocatalytic activity.

The regulation of the energy band structures is the best way to enhance the visible light photocatalytic performance, generally by doping, defects engineering, and surface modification.

Li et al. attribute the increased efficiency of Carbon doped TiO<sub>2</sub> nanofiber under visible light to the presence of oxygen vacancies at the surface while the Ti terminals act as reaction sites, resulting in the accumulation of CO\* intermediates to produce CH<sub>4</sub> [60]. The role of C doping is further analyzed by Nor et al., By DFT calculations. They suggest that C-doped O sites are more stable in bulk than in the subsurface or on the surface, while C-doped Ti sites are more stable on the surface than in the bulk or subsurface. While the presence of C in the O sites introduces impurity states in the band gap that do not affect the band gap energy but induce the formation of electron traps, Carbon in Ti sites induces structural distortions with a reduction in the band gap energy. Both doping processes enhance light absorption in the visible and IR spectrum [61]. The role of lanthanides as doping elements and/or surface modification has been widely studied. The presence of Dy generates a ligand-to-metal charge transfer process in the visible region (500–600 nm), lowering the bandgap to ~2.24 eV [62]. Guetni et al. found that doping TiO<sub>2</sub> with Nd allows the material to absorb radiation in the visible range by creating Nd-4f impurity states. The co-doping with Y further increases the Azo dye orange G degradation under a wavelength range of 300–800 nm due to the synergetic effect of intragap levels [63].

The increased visible-light photoactivity of metal-doped TiO<sub>2</sub> by intragap levels in the semiconductor band gap requires photons with lower energy to produce carriers in the conduction band. It is well known that in N-doped TiO<sub>2</sub>, the lowered band gap is due

to the formation of N-2p state hybrids with O-2p states in the anatase phase [64]. Further, the improved trapping of electrons at oxygen vacancy sites can inhibit the electron-hole recombination resulting in enhanced photo-activity [65].

A different mechanism is related to the formation of Oxygen vacancies at the surfaces of the semiconductors (related to metallic doping) and, consequently, to F centers with different charges. The loss of an O atom in a metal oxide generates an electron pair trapped in VO (F center), while a positively charged F<sup>+</sup> center is due to a single electron in the O vacancy. An unsaturated vacancy generates an F<sup>++</sup> center [66]. The presence of charge defects strongly increases the surface reactivity and, as a consequence, the photocatalytic activity, too.

Various metal nanoparticles such as Pt, Au, Pd, Ru, Rh, and Ag have been employed in implementing the semiconductor surface to achieve higher photocatalytic efficiency. High energy irradiation induces Fermi-level equilibration between the semiconductor (like TiO<sub>2</sub>) and the metal element through charge distribution [67,68], strongly increasing the electron transfer on the semiconductor/metal interfacial system and promoting efficient photocatalytic reactions. The presence of resonance factor related to the reduced dimension of the metal nanoparticle at the surface (mainly Au and Ag) can give act as an added mechanism.

A different approach consists of the use of carbon aerogels materials hybridized with TiO<sub>2</sub>; the main effect is related to the increase in the surface area of TiO<sub>2</sub> due to the great porosity and highly developed hierarchical porous structures. Further, Carbon functionalization results in the formation of new intragap levels that red-shift the absorption in the visible range and, acting as a charge trap, limit the recombination rate [58]. However, there are still some issues to be solved, firstly, the efficiency in the photodegradation should be still increased, but mainly there are some issues related to the synthesis procedure that requires intensive energy consumption and the use of a considerable amount of organic precursor such as formaldehyde [69].

Localized surface plasmonic resonance (LSPR) can be seen as the collective free electron charge oscillation in the metallic nanoparticles optically consistent with the frequency of the incident light wave [70]. This phenomenon usually occurs in nanoparticles below 50 nm and creates an added optical excitation band in the visible region (480 for Ag, 520 for Au) [71].

Yukika et al. coupled small Pt nanospheres with large Au nanocubes on TiO<sub>2</sub> to obtain a coupling resonance mode at about 600 nm. Further, the bimetallic coupling allowed charge separation and catalytic reaction at the Pt site and a light-harvesting antenna at the Au site, respectively [72].

It was observed that catalytic reduction of CO<sub>2</sub> can be obtained with Au nanoparticles deposited TiO<sub>2</sub> under full solar-spectrum irradiation, thanks to the visible contribution associated caused with the LSPR effect of Au NPs [70,73]. A further method to increase the photo-efficiency foresaw the synergic effect of the localized plasmonic features and the formation of metal chiral structures. Indeed, plasmonic materials with chiral configurations have not only emulated the optical properties of their molecular counterparts, but the chiroptical activity can achieve 10 orders of magnitude greater [74,75]. The great enhancement of the electric field, as well as the formation of hot injecting electrons in the semiconductor inside and around the plasmonic nanostructures, are the main player in the mechanism.

Organic semiconductors have recently gained large interest due to the earth's abundance of their constituent elements, optical and structural properties, and in particular, their tunable energy levels. It is outside the scope of the present paper, but interesting examples of reviews on the use of organic semiconductors in photocatalytic applications are reported in Refs. [76,77].

This class of materials can be divided into two categories: polymers and small molecule materials. Polymeric macro-molecules are constituted by the repetition of a fundamental unit (monomer) and are based on *sp*<sup>2</sup> hybridized carbon atoms, with the alternation of single and double bonds along their building block (Figure 6).

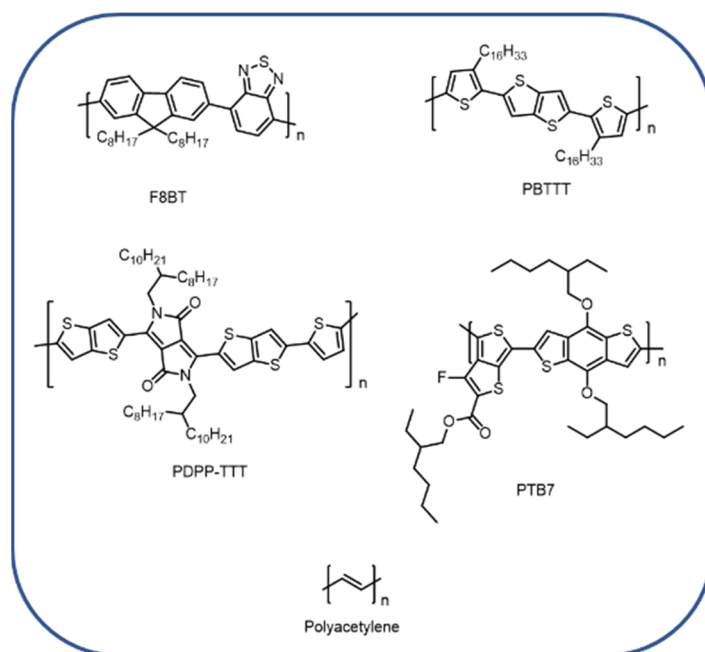


**Figure 6.** Chemical structures of polymeric semiconductors.

Within the organic chemistry panorama, polymers can guarantee very high versatility in terms of structural and optical response with high potential in several applications [78–80], but their efficiency is hampered by the low thermal and short-time structural stability of the compounds (Figure 7).

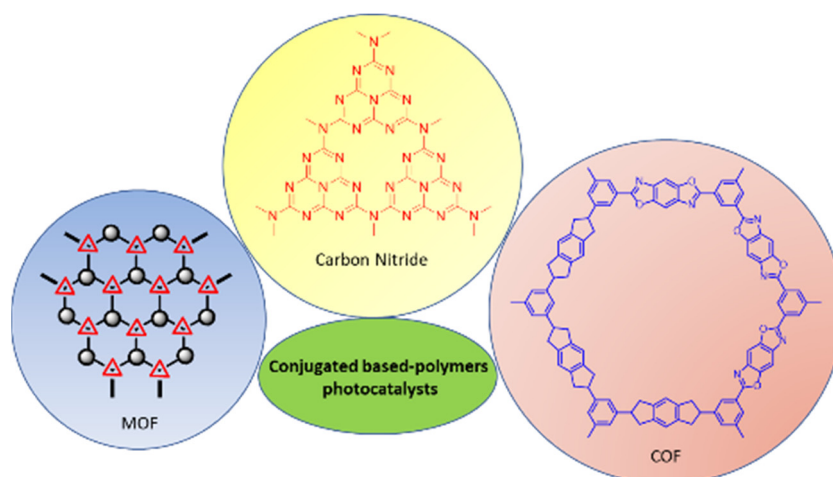


**Figure 7.** Examples of conjugated polymer photocatalysts.

Covalent organic frameworks (COFs) are a type of purely organic crystalline porous polymeric material with a very high structural tunability due to the high possibility of varying the various functional building blocks [81,82]. COF can be tuned to vary the absorption into the visible range up to infrared with relatively high efficiency. Further, the large specific surface area and regular and customizable micro- and mesopores can offer increased interaction between substrates and catalytic sites. Furthermore, via bottom-up synthesis, post-modification, doping, photosensitization, and hybridization with other photoactive compounds, the construction of the heterojunction structure, the electron-hole recombination can be greatly retarded, the charge transfer processes can be accelerated, and the charge transfer resistance can be greatly decreased [12]. Moreover, the considerably

large specific surface area and numerous regular and customizable micro- and mesopores can offer favourable guest-host interaction between substrates and catalytic sites. The building blocks to produce the organic porous architectures are generally rigid and do not possess bulky side groups.

In this scenario, polymeric carbon nitrides have emerged as promising materials for being metal-free semiconductors and metal-free photocatalysts.

First attempts to prepare solid-state carbon nitride materials have been known in the literature since early 1830, and they have eluded rigorous analyses and characterizations for a long time because of their insolubility in water and organic solvents.

Kroke et al., using density functional theory methods (DFT), proposed a polymer based on two-dimensional tri-s-triazine units (heptazines) as the most thermodynamically stable structure of carbon nitride [83]. This polymer, because of its graphitic-like structure, was then called and studied graphitic carbon nitride ( $g\text{-C}_3\text{N}_4$ ) and has attracted strong attention because of its tunable optoelectronic properties and because it is a metal-free semiconductor [84–86]. The chemical structure of graphitic carbon nitride has been deeply studied with different techniques, including solid-state nuclear magnetic resonance spectroscopy, Fourier-transform infrared spectroscopy, and x-ray diffractometry [87]. These studies confirmed that  $g\text{-C}_3\text{N}_4$  is a layered material, in which van der Waals force holds the stacking layers (C-N bonds), and each layer is composed of tri-s-triazine units, bridged by tertiary amino groups with a high degree of condensation. It is thermally and chemically stable under ambient conditions, biocompatible, eco-friendly, and the graphite-like planar configuration, with a  $\pi$  conjugated system, thereby enabling the transport of charge carriers, and the moderate bandgap makes it workable in the visible part of the solar spectrum [88–91]. The lone pair electrons of nitrogen are responsible for the formation of the lone pair valence band and the band structure. The combination of the lone pair state and the p bonding stabilizes the lone pair position becoming the key to the electronic structure [92,93].

These appealing properties make  $g\text{-C}_3\text{N}_4$  useful for different applications, and from 2000–2019, around 5100 publications have been published on  $g\text{-C}_3\text{N}_4$  applications, including photocatalytic water splitting,  $\text{CO}_2$  reduction, environmental remediation, organic transformation, and white light-emitting diodes [19,94].

Despite these positive attributes, the efficiency of  $g\text{-C}_3\text{N}_4$  as a standalone photocatalytic material is diminished by a low quantum efficiency and high recombination rate of photogenerated electron-hole pairs [95]. However, the modification of  $g\text{-C}_3\text{N}_4$  could overcome these problems. Recent studies reported that by controlling the morphology and the surface properties of these catalysts, a significant enhancement in photo-reduction is observed. In particular, Porcu et al. studied a new polymer of the family of carbon nitrides with enhanced absorption in the visible part of the solar spectrum [96]. They showed how the protonation method could improve the solubility, dispersibility, and electronic structure, and the exfoliation method of 2D structures, through the breaking of Van der Waals forces, can improve light absorption (Figure 8) [97].

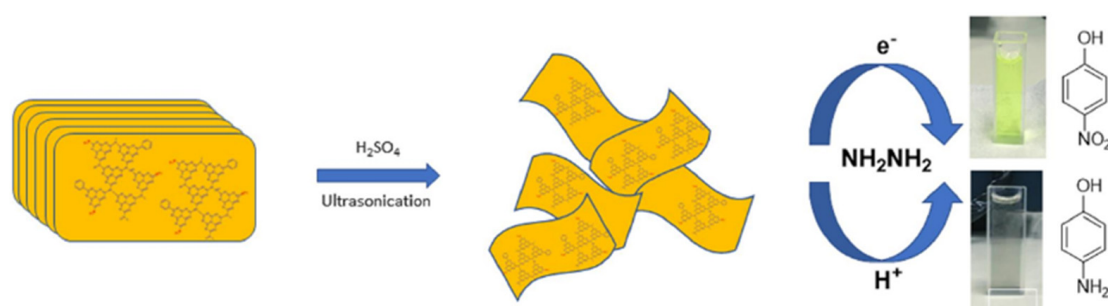


**Figure 8.** 4–Nitrophenol reduction using protonated and exfoliated phenyl carbon nitride (pePhCN) as photocatalyst [97].

#### 4. Heterostructures

One of the most effective strategies for improving the photocatalytic efficiency of semiconductor materials is the design of heterojunction systems [98–100]. A general rational design and fabrication of heterojunction photocatalysts, such as the semiconductor–semiconductor heterojunction, the semiconductor–metal heterojunction, the semiconductor–carbon heterojunction, and the multicomponent heterojunction can be found in the review of Wang et al. [101].

Heterojunction photocatalysts are obtained by coupling two semiconductor photocatalysts and taking advantage of their relative band structure [102,103]. The coupling of the two systems has been classified into Type I, Type II, Z, and S-scheme photocatalysts. (Figure 9) [29,98].

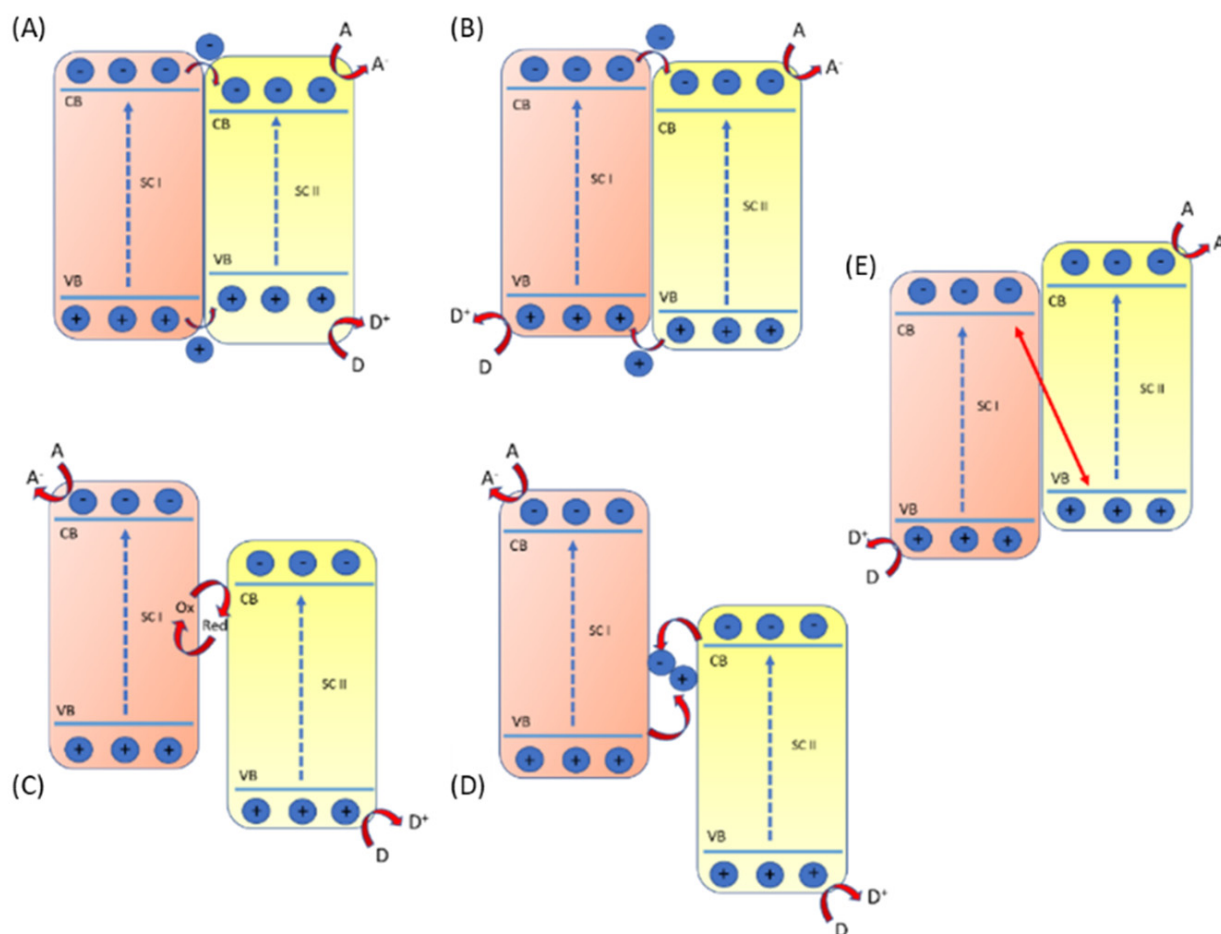


**Figure 9.** Heterostructures. (A) type-I (B) type-II (C) Z-scheme with redox mediator (D) all solid Z-scheme (E) S-scheme.

In type I, the heterostructure is formed by two semiconductors, and the photoinduced electron and holes are transferred from one semiconductor to the other, but due to the electron-holes accumulation in one semiconductor, the redox ability is relatively low. Type-II heterojunction has been widely studied and applied, starting in the 1980s [104]. It is based on the simultaneous formation, upon a proper excitation wavelength, of electrons and holes in both photocatalysts. Photogenerated electrons were transferred from one photocatalyst to the other, while photogenerated holes were transferred in the opposite direction. Thus, the photogenerated carriers are spatially separated, and electrons and holes accumulate on different photocatalysts, one for the reduction reactions and the other for oxidation reactions, respectively.

Despite the interesting process and the wide application and studies applied in this scheme [105], the type II scheme presents a low redox ability. Actually, from a dynamic per-

spective, the repulsion from the existing carrier (electron and carrier) already accumulated in one photocatalyst hampered the transfer process, weakening the overall redox ability of the heterojunction [106,107].

The Z-scheme composites show a high redox potential and very efficient charge carrier separation. The photoinduced holes of semiconductor I recombine with the photoinduced electrons of semiconductor II leaving the photoinduced electrons of semiconductor I and the photogenerated holes of semiconductor II free to be active in the reduction and oxidation process, respectively [108]. These kinds of heterostructures find application in many fields, such as CO<sub>2</sub> conversion, water splitting, and pollutant degradation [56,109,110].

The concept of the “direct Z-scheme” has been developed gradually. One of the first successful applications was the dye-sensitized TiO<sub>2</sub> by Gratzel [110], where a tandem cell was obtained by coupling nanocrystalline WO<sub>3</sub> or Fe<sub>2</sub>O<sub>3</sub> with dye-sensitized TiO<sub>2</sub>. In this case, holes in the valence band of WO<sub>3</sub> or Fe<sub>2</sub>O<sub>3</sub> generated by UV radiation are involved in a water oxidation reaction, while the electrons, transferred to dye-sensitized TiO<sub>2</sub>, will generate hydrogen in the water reduction reaction. Further, Balayeva et al. developed a surface-grafted WO<sub>3</sub>/TiO<sub>2</sub> hybrid system with high photoactivity under visible light irradiation for indoor air purification [111]. Another Z-scheme application is ZnO-CdS Z-scheme heterojunction for improved H<sub>2</sub> evolution performance and, more recently, Cu<sub>2</sub>O-Pt/SiC/IrOx heterostructure for CO<sub>2</sub> reduction and O<sub>2</sub> evolution [112]. Indeed, the second generation of Z-scheme photocatalysts considers the use of a mediator between the two materials. The close contact between the photocatalysts and the mediator allows the faster recombination between the photogenerated carriers (electrons from PS II with the photogenerated holes from PS I) due to a lower contact resistance interface [113].

Recently a new scheme has been proposed, the so-called S-Scheme. An S-scheme is like a type-II heterojunction but with a different charge-transfer path. In a typical type-II heterojunction, photogenerated electrons and holes are accumulated on the conduction band and valence band of the two semiconductors resulting in weak redox ability. In an S-scheme heterojunction, the photogenerated electrons and holes are stored in the conduction band of the reduction photocatalysts and the valence band of the Oxidative photocatalyst, respectively, while the other photogenerated charge carriers of the two semiconductors are recombined together [98].

Jang et al. [114] report superior performances for H<sub>2</sub>O<sub>2</sub> production in a heterojunction between ZnO and WO<sub>3</sub>. The formation of the S-scheme heterojunction (ZnO and WO<sub>3</sub>) generates electrons on the conduction band of ZnO and holes on the valence band of WO<sub>3</sub> that are efficiently spatially separated. Further, CdS/TiO<sub>2</sub> heterostructures with a working s-scheme are reported by Wang et al. Due to the higher different working function, electrons from CdS can transfer to TiO<sub>2</sub>, forming the internal electric field directing from CdS to TiO<sub>2</sub>. Under illumination, the photogenerated holes in the valence band of CdS recombine with the photogenerated electrons in the conduction band of TiO<sub>2</sub> driven, leaving the photogenerated carriers (electron in the conduction band of CdS and photogenerated holes in the valence band of TiO<sub>2</sub>) free to act to the CO<sub>2</sub> reduction and water oxidation reactions, respectively [115].

The S-scheme has been highly utilized in the hybrid organic-inorganic heterostructures, and it will be recalled in the following paragraph.

## 5. Organic/Inorganic Heterostructures

The development of new materials with higher activity and versatile properties for photocatalytic applications is strongly required. The formation of “hybrid materials”, by coupling an inorganic material (often already in the list of the classical photocatalysts) with new organic structures (often represented by stable polymers) permits to obtain a new class of materials with superior and tunable properties (Figure 10).

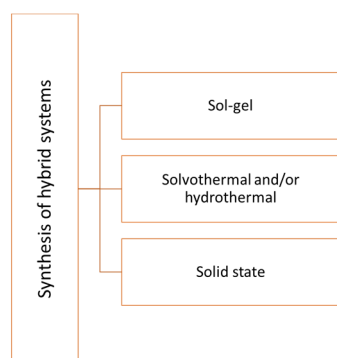


**Figure 10.** Most representative synthetic methods to obtain hybrid systems.

Depending on the type of bonding between the two materials, different effects and classifications can be defined. In the first case, the stability of the structure is provided by the presence of physical interactions, such as hydrogen bonding, van der Waals force, or ionic interactions. Proper functional groups at the surface are necessary to stabilize the interaction and stabilize the structure. The second type is defined by stronger interactions generated by chemical bonding, and in general, it defines very stable hybrid materials and a fast charge transfer process.

The organic part in the hybrid system can either be molecular catalysts or organic dyes, which can act as photocatalysts or sensitizers. In this latter case, they will not act as a photocatalyst but support the new system with their properties. The general mechanism is relatively easy: the sensitizer, chemically adsorbed on the semiconductor surface, absorbs the photon with a suitable wavelength passing to an excited state, then the photoexcited carriers are injected into the excited inorganic band (following one of the above described mechanism, such as Z-scheme and/or S-Scheme). The main scope of the sensitizer is to overcome the physical limitations of the inorganic semiconductors, which generally can absorb only the UV component of the electromagnetic spectrum. Different systems were proposed, where both the inorganic part as well the organic units have been varied. Metal oxides still represent the most common choice, while much more variety can be found in the organic choice.

The  $\pi$ -conjugated systems are promising materials as sensitizers in hybrid systems. Suárez-Méndez et al. [116] report the increased photocatalytic performance of protonated thiophene-based oligomers (OTn<sup>+</sup>) as sensitizers in an OTn/TiO<sub>2</sub> system, while Zhong et al. show high H<sub>2</sub> production activity using excitation wavelengths greater than 420 nm in a porous organic-inorganic hybrid system formed by Calix [4] arene dye as sensitizer and titanium dioxide as acceptor units [117].

Coumarins represent a further interesting material for the high absorption cross-section and guarantee an efficient and fast charge transfer to TiO<sub>2</sub> through the LUMO level to the conduction bands [118,119], but generally have low structural stability and long-time performances. Hence, among the different organic units, the choice of polymers could generally guarantee increased stability. In particular, the organic-inorganic hybrid system that couples TiO<sub>2</sub> to graphitic carbon nitride (g-C<sub>3</sub>N<sub>4</sub>) represents an intriguing solution because it meshes the photocatalytic properties of TiO<sub>2</sub> with the lower band gap energy (2.7 eV) and thermal and chemical stability of g-C<sub>3</sub>N<sub>4</sub> [120,121]. Two-dimensional conjugated polymers have emerged as a promising class of materials for photocatalytic applications thanks to their photo-physical properties such as: being eco-friendly, consisting of heart-abundant elements, easiness of synthesis, and chemically stable. Additionally, the delocalized conjugated structure of g-C<sub>3</sub>N<sub>4</sub> gives rise to a slow charge recombination rate and a rapid photoinduced charge separation. The formation of a charge-transfer complex at the interface between the organic donor (i.e., g-C<sub>3</sub>N<sub>4</sub>) and inorganic acceptor (i.e., TiO<sub>2</sub>) compound results in a g-C<sub>3</sub>N<sub>4</sub>/TiO<sub>2</sub> heterojunction system that shows a decrease in the recombination rate of photogenerated electron-hole pairs, as well as an increase in the pho-

photocatalytic activity of TiO<sub>2</sub> under visible light for wavelengths as low as 450 nm [122–125]. The band scheme of the band structure of TiO<sub>2</sub>/g-C<sub>3</sub>N<sub>4</sub> can be seen as an efficient Z-scheme where the internal electric field directing from g-C<sub>3</sub>N<sub>4</sub> to TiO<sub>2</sub> was formed because of their different work functions.

Rodrigues et al. reported a photocatalytic activity under visible radiation of the TiO<sub>2</sub>/g-C<sub>3</sub>N<sub>4</sub> improved by 44.8% compared to pure TiO<sub>2</sub>, whereas an improvement of 30.5% was obtained under simulated solar radiation, generated by the creation of an effective Z-scheme heterojunction [126]. Further, Liu et al. develop a supramolecular self-assembly approach combined with thermal polycondensation to construct direct Z-scheme-dictated TiO<sub>2</sub>/g-C<sub>3</sub>N<sub>4</sub> heterojunctions. The hybrid porous nanostructures possess hydrogen-bonded interfacial contact between TiO<sub>2</sub> and g-C<sub>3</sub>N<sub>4</sub> with enhanced visible-light photocatalytic activity in the degradation of phenolic pollutants, acetaminophen, and methylparaben, in comparison to the pure TiO<sub>2</sub> and g-C<sub>3</sub>N<sub>4</sub> [127].

The heterostructures WO<sub>3</sub>/g-C<sub>3</sub>N<sub>4</sub> represent the application of an S-scheme, useful for hydrogen production [128]. In this scheme, similar to the previous example, the work function of WO<sub>3</sub> (6.23 eV) is larger than that of g-C<sub>3</sub>N<sub>4</sub> (4.18 eV), inducing the formation of an internal electric field from the polymer to the inorganic semiconductor and band-edge bending due to electron redistribution. Upon excitation, the photogenerated holes in the valence band of g-C<sub>3</sub>N<sub>4</sub> recombine with the electrons in the conduction band of WO<sub>3</sub>, leaving the photogenerated carriers (electron of g-C<sub>3</sub>N<sub>4</sub> and holes of WO<sub>3</sub>) free to participate in photocatalytic reactions. Following a similar scheme, CeO<sub>2</sub> quantum dots (QDs) intimately anchored on a g-C<sub>3</sub>N<sub>4</sub> have been successfully utilized for a heterostructure with efficient photocatalytic performance for bacteria disinfection [129].

ZnS nanoparticles (10–15 nm) hybridized with g-C<sub>3</sub>N<sub>4</sub> showed photocatalytic hydrogen evolution using glucose as the substrate. Interestingly, different efficiency has been observed depending on the synthesis method of Carbon nitride (melamine, urea, and dicyandiamide). The best yield was obtained from g-C<sub>3</sub>N<sub>4</sub> produced from melamine [130].

A further application of g-C<sub>3</sub>N<sub>4</sub> in the hybrid systems is provided by g-C<sub>3</sub>N<sub>4</sub>/Ag<sub>2</sub>CO<sub>3</sub> heterostructures. The photocatalytic experiments indicated that the g-C<sub>3</sub>N<sub>4</sub>/Ag<sub>2</sub>CO<sub>3</sub> photocatalyst exhibited significantly enhanced photocatalytic activity than the pure g-C<sub>3</sub>N<sub>4</sub> and Ag<sub>2</sub>CO<sub>3</sub> samples toward degrading methyl orange (MO) and catalytic ozonation for oxalic acid mineralization, under visible light irradiation ( $\lambda > 420\text{nm}$ ) [131,132].

The ZnO/K-CN hybrid exhibits excellent photocatalytic degradation and adsorption efficiency of tetracycline under simulated sunlight, and the degradation rate reaches 90% due to the synergetic action of the formation of efficient type-II heterojunction between the K-doped exfoliated g-C<sub>3</sub>N<sub>4</sub> nanosheet (K-CN) and the ZnO nanorod and the adsorption capacity of tetracycline through electrostatic force [133].

The ZnO/g-C<sub>3</sub>N<sub>4</sub> hybrid system was successfully utilized as a sensor with high selectivity to dimethylamine (DMA), fast response time, and a fast recovery time. The heterojunction is effective for electron transfer and adsorption of oxygen molecules forming reactive oxygen species and thereby promoting the reaction between oxygen and DMA [134].

The use of metal complexes and metal nanoparticles (Au, Pt, Ag, etc.) in exfoliated carbon nitrides was utilized in the recent year for the successful application of photocatalysis. The nanosized metal particle will provide an extra absorption band related to localized surface plasmon resonance in the visible region and the possibility of injecting hot carriers into the reaction. Ag/C<sub>3</sub>N<sub>4</sub> photocatalysts exhibited excellent stability and enhanced visible-light-driven photocatalytic performance both in the degradation of methyl orange (MO) and H<sub>2</sub> evolution from water splitting [135]. Wang et al. found that under visible light illumination, the Au/g-C<sub>3</sub>N<sub>4</sub> hybrids catalyst exhibits a superior oxygen evolution reaction performance in alkaline electrolytes. The high activity was attributed to three factors: the hot electrons injection of localized surface plasmon effect induced by light illumination and the formation of Schottky heterostructure [136]. The formation of heterojunctions between AgCl/ZnO and g-C<sub>3</sub>N<sub>4</sub> significantly increases electron-hole transfer

and separation compared to pure ZnO and g-C<sub>3</sub>N<sub>4</sub>. Thus, AgCl/ZnO/g-C<sub>3</sub>N<sub>4</sub> exhibits increased photocatalytic activity in the removal of tetracycline hydrochloride, reaching 90 % under visible light irradiation. Hydrogen peroxide (H<sub>2</sub>O<sub>2</sub>) and superoxide radical ( $\cdot\text{O}_2$ ) contributed more than holes (h<sup>+</sup>) and hydroxyl radicals ( $\cdot\text{OH}$ ) to the degradation process [134]. Zhang et al. observed that, contrary to pure g-C<sub>3</sub>N<sub>4</sub>, direct splitting of pure water is achieved with graphitic carbon nitride modified with Pt, PtO<sub>x</sub>, and CoO<sub>x</sub> as redox cocatalysts [137]. The photoactivity of Au/g-C<sub>3</sub>N<sub>4</sub> nanocomposites showed higher efficiency in the degradation of both methylene blue dye and the gemifloxacin mesylate compared with that of bare g-C<sub>3</sub>N<sub>4</sub>. The efficiency was evaluated as a function of relative concentration between gold and g-C<sub>3</sub>N<sub>4</sub>, indicating the 1%Au/g-C<sub>3</sub>N<sub>4</sub> nanocomposites as the best among the samples studied. Under visible excitation, it was able to reach more than 95% degradation of the target dye molecule in 90 min, in contrast to less than 70% obtained by pure g-C<sub>3</sub>N<sub>4</sub> [138].

The structure of the hybrid photocatalysts can be arranged in more articulated paths, like a plasmonic ternary hybrid photocatalyst of Ag/AgBr/g-C<sub>3</sub>N<sub>4</sub>, synthesized and used for water splitting under visible light irradiation. Compared to a simple mixture of Ag/AgBr and g-C<sub>3</sub>N<sub>4</sub>, the ternary heterostructure showed a higher photoactivity. The performances are increased thanks to different factors: the decreasing of the recombination rate into the polymeric structure due to the high separation of the photoexcited charge, the low dimension of the Ag/AgBr nanoparticles, and the enhanced absorption related to the plasmonic resonance in the visible region [139]. Further, an efficient Ag/Ag<sub>2</sub>WO<sub>4</sub>/g-C<sub>3</sub>N<sub>4</sub> ternary plasmonic photocatalyst was successfully synthesized using a facile one-step in situ hydrothermal methods. The strong coupling effect between the Ag/Ag<sub>2</sub>WO<sub>4</sub> nanoparticles and the exfoliated g-C<sub>3</sub>N<sub>4</sub> nanosheets gives excellent photocatalytic results (Rhodamine B and tetracycline degradation) under visible-light excitation thanks to the synergic action of the reduced the recombination rate of photogenerated electrons and holes and plasmonic absorption [140].

The metal can play the role of a cocatalyst, too, lowering the activation energy and increasing the rate of hydrogen production. Metals such as Pt, Au, Ag, Rh, and Ni are widely used as a cocatalyst to increase the efficiency of C<sub>3</sub>N<sub>4</sub> for hydrogen evolution [141].

In Pt/g-C<sub>3</sub>N<sub>4</sub>-GO photocatalysts, the H<sub>2</sub> evolution activity is strongly influenced by the temperature of the reduction stage, so the maximal rate of H<sub>2</sub> evolution was obtained for the catalyst reduced at 400, and Pt concentration of 0.5%. The quantum efficiency was about 3% [142].

The photoactivity of Au/g-C<sub>3</sub>N<sub>4</sub> nanocomposites has been evaluated for the degradation of both methylene blue dye and the drug Gemifloxacin mesylate, and their efficiencies were compared with that of bare g-C<sub>3</sub>N<sub>4</sub>. The efficiency increased by over 95% destruction of the target dye molecule in 90 min, in contrast to the 69% achieved with bare g-C<sub>3</sub>N<sub>4</sub> [138].

Surface plasmon resonance plays a fundamental role in the visible photocatalytic property and photoinduced electron-hole pair separation efficiency. Ag-decorated g-C<sub>3</sub>N<sub>4</sub> reports high photocatalytic degradation efficiency of methyl orange (98.7% within 2 h) and the high catalytic reduction property of 4-nitrophenol (100% within 70 s) [143].

Au/g-C<sub>3</sub>N<sub>4</sub>/NiFe<sub>2</sub>O<sub>4</sub> exhibited a significant visible-light-driven photoactivity for hydrogen production. The high photocatalytic performances of the ternary hybrid nanocomposites are related to the high visible absorbance for charge carrier production, the fast separation of the electrons captured by AuNPs, and the strong absorption at the localized surface plasmon band in the Au nanoparticles that generate high-density carriers under visible light irradiation [144].

A new class of hybrid photocatalysts is constituted by metal-organic frameworks (MOF), generally constituted by porous crystalline materials with metallic nodes (metal ions or clusters) and organic linkers. MOFs have recently attracted increasing attention in the field of photocatalysis for their ultra-high specific surface area (over 6000 m<sup>2</sup>g<sup>-1</sup>), rich topology, and easily tunable porous structure [145].

In some MOFs, the metal clusters and organic linkers can be regarded as isolated semiconductor quantum dots, while the organic framer act as a light-absorbing antenna [146].

Structures such as MOF-5 ( $Zn_4O(BDC)_3$ , BDC: 1,4-benzenedicarboxylate),  $(Zr_6O_4(OH)_4(BDC)_6)$ , and  $Ti_8O_8(OH)_4(BDC)_6$ , displayed semiconductor-like behavior. Herein, the metal-oxo clusters and organic linkers can be regarded as isolated semiconductor quantum dots and light-absorbing antennae, respectively.

In MOF structures, the HOMO/LUMO levels play similar roles as the conduction and valence band in classical semiconductors. The photogenerated electrons in the LUMO can be transferred to  $O_2$ , leading to the formation of superoxide radicals ( $O_2^{\cdot-}$ ). Meanwhile, holes in the HOMO can oxidize the surface hydroxyl group/water, generating hydroxyl radicals ( $HO^{\cdot}$ ). The band gap of MOF can be modeled in a very wide range, from 3 to 4 eV MOF-5, UiO-66(Zr), and MIL-125(Ti) to a band gap lower than 2 eV in Fe- based MOF. In order to increase the photocatalytic efficiency in the visible region, different strategies have been proposed, mainly devoted to the generation, separation, and transfer of charge carriers [147]. The most studied technique to tune the optical properties is the modification of organic linkers rather than metallic modes. As an example, the use of  $-NH_2$  groups in  $H_2BDC$  decreases the absorption edge down to 2.45 eV, whereas in pure  $H_2BDC$ , the band gap is 3.6 eV, thereby extending the efficiency in the visible part of the spectrum [148].

Remarkably, the introduction of the  $-NH_2$  group leads to increased energy of the HOMO level with no influence on the LUMO. Similar effects have been studied for other functional groups where the  $-(NH_2)_2$  group is the most active one:  $-CH_3/-Cl < -OH < -(NH_2)_2$  [149]. Similarly, it is possible to use the Covalent organic framework (COF) to obtain efficient visible photocatalysis. In MOF/COF heterostructured photocatalyst (Cu- $NH_2$ -MIL-125/TpPa-2-COF), with Cu ions immobilized by  $-NH_2$  groups of MOF, while the covalently connected heterojunction facilitates the separation of photogenerated charges. The results show an efficient “amines to imines” process with a high conversion rate (91.2%) and selectivity (>99%) [150].

In addition to functional group modification, the implantation of transition metal ions to complexes with ligands was reported to be a feasible way to enhance photocatalytic performance [151]. The implantation of  $Fe^{3+}$  in porphyrinic MOFs (PCN-224) generates an extension of the optical response to a longer wavelength inhibiting the recombination of electron-hole pairs. Lou et al. report sheet-like sliver vanadate/Bi-Fe MOF (AGV/HBF) heterojunction composite with superior efficiency under visible light irradiation (almost 99% in 2 h for the photocatalytic decomposition of Rhodamine B). The enhanced photocatalytic performance was attributed to the strong visible-light absorption and low recombination of electron-hole pairs due to the as-formed heterojunctions [152].

The dye-sensitizing approach is applied even to the MOF structure. The high specific area and the high number of bonding sites can facilitate a strong interaction and an efficient antenna effect of the dyes. The dye/MOF structure has been applied to  $H_2$  production and  $CO_2$  reduction, and environmental remediation [152].

Li et al. report porous copper-based metal-organic framework (Cu-MOF) tailored by encapsulating visible-light photosensitive dyes. The study underlying the high-efficiency and diversified performances of the different systems in the photodegradation process reveals significant achievements in tailoring the photocatalytic capabilities via introducing dyes with different photosensitivity into an identical porous copper-organic framework [153].

The coupling of MOFs with other photoactive semiconductors represents an additional strategy to enhance photocatalytic activity. Again, the high specific area of the MOF structure facilitates this approach. Three types of heterojunctions for semiconductors can be identified, depending on the relative position of the Conduction and Valence band as well as the n/p characters of the independent components, namely straddling gap; type-II: staggered gap; type-III: broken gap [101,154]. Until now, many semiconductors have been reported to form composites with MOFs. Metal-containing semiconductors (such as ZnO [155],  $TiO_2$  [156],  $BiVO_4$  [157], and CdS [158]) and non-metal graphitic carbon

nitride [159] have been reported to form composites with MOFs exhibiting highly potential performance in the field of photocatalysis.

Doustkhah et al. utilized the highly porous structure of the MOF (MOF-5) as a precursor to obtaining superior photocatalytic activity in degrading methylene blue (MB) in comparison to other ZnO nanostructures [155]. Similarly, CdS/Cd-MOF nanocomposites were constructed by in situ sulfurizations to form CdS using Cd-MOF as a precursor. The role of the high specific surface is evidenced by the high degradation rate of MB (91.9%) in comparison with the pure Cd-MOF (62.3%) and pure CdS (67.5%) [158].

## 6. Organic/Inorganic Heterostructures: Applications

Organic-Inorganic hybrids have been widely studied as efficient photocatalysts, degradation of organic pollutants, hydrogen evolution, CO<sub>2</sub> reduction, sterilization, and reduction of heavy metals are the most studied. In Table 1 are collected some examples of hybrid photocatalysts for each application.

**Table 1.** Organic-Inorganic photocatalysts and applications.

Application	Photocatalyst	Photocatalysts Target	Source of Light	Efficiency	Ref.
Degradation of organic pollutants	Citric acid/CeO <sub>2</sub>	50 mgL <sup>-1</sup> glyphosphate	UV lamp 800 W/m <sup>2</sup> , 365 nm and visible lamp 1800 W/m <sup>2</sup> , 400–800 nm	100%	[160]
	Perylene imide/Bi <sub>2</sub> WO <sub>6</sub>	50 mL Bisphenol A 10 ppm	300 W Xe lamp cold light source	100%	[161]
	Ag <sub>3</sub> PO <sub>4</sub> /PDI	20 mgL <sup>-1</sup> tetracycline hydrochloride	300 W xenon lamp with a cut filter (>420 nm)	82%	[162]
	WO <sub>3</sub> /Cu/PDI	20 mgL <sup>-1</sup> tetracycline hydrochloride	300 W Xe lamp with a cut-off filter ( $\lambda > 420$ nm)	75%	[163]
	ZnSe/Polyaniline	10 mgL <sup>-1</sup> tetracycline hydrochloride	LED with 50 W powers and 4300 LM as a visible-light source	90%	[164]
	g-C <sub>3</sub> N <sub>4</sub> /TiO <sub>2</sub>	200 mL Bisphenol A, Brilliant green and mixed dyes 20 mgL <sup>-1</sup>	Direct sunlight	95%	[165]
	PhCN/TiO <sub>2</sub>	50 mL RhB/MB 10 mgL <sup>-1</sup>	white LED Philips 13 W with optical power 100 mW	98%	[166]
Hydrogen evolution	S-doped g-C <sub>3</sub> N <sub>4</sub> /TiO <sub>2</sub>	100 mL Congo Red 50 mgL <sup>-1</sup>	300 W Xenon lamp	>90%	[167]
	Polyaniline/ZnO	H <sub>2</sub> O	Xenon lamp	9.4 mmolh <sup>-1</sup> g <sup>-1</sup> H <sub>2</sub>	[168]
	Cds/TCP	H <sub>2</sub> O	300 W Xe-lamp UV cut-off filter $\lambda \geq 420$ nm	104.51 mmolh <sup>-1</sup> g <sup>-1</sup> H <sub>2</sub>	[169]
	Pyrene/MoS <sub>2</sub>	H <sub>2</sub> O	A 300 W Xe lamp with a working current of 15 A	2.7 mmolh <sup>-1</sup> g <sup>-1</sup> H <sub>2</sub>	[170]
	Ti-phosphonate/MOF	H <sub>2</sub> O	visible-light irradiation ( $\lambda > 400$ nm)	1260 mmolh <sup>-1</sup> g <sup>-1</sup> H <sub>2</sub>	[171]
CO <sub>2</sub> reduction	gC <sub>3</sub> N <sub>4</sub> /TiO <sub>2</sub> /Ti <sub>3</sub> C <sub>2</sub>	H <sub>2</sub> O	simulated visible light (Xe 300 W lamp)	2592 $\mu$ molh <sup>-1</sup> g <sup>-1</sup> H <sub>2</sub>	[172]
	InVO <sub>4</sub> /g-C <sub>3</sub> N <sub>4</sub>	CO <sub>2</sub> and H <sub>2</sub> O	visible light irradiation ( $\lambda > 420$ nm)	69.8 mmolh <sup>-1</sup> g <sup>-1</sup> CO	[173]
	Graphydine/Bi <sub>2</sub> WO <sub>6</sub>	CO <sub>2</sub> and H <sub>2</sub> O	simulated sunlight irradiation	2.13 mmolh <sup>-1</sup> g <sup>-1</sup> CH <sub>3</sub> OH	[174]
	Zr(IV)/MOF/Co	CO <sub>2</sub> and H <sub>2</sub> O	visible-light irradiation	70.8 mmolh <sup>-1</sup> g <sup>-1</sup> CH <sub>4</sub>	[175]
	SnNb <sub>2</sub> O <sub>6</sub> /CdSe-DETA	CO <sub>2</sub> and H <sub>2</sub> O	visible-light irradiation ( $\lambda > 400$ nm)	36.16 mmolh <sup>-1</sup> g <sup>-1</sup> CO	[176]
g-C <sub>3</sub> N <sub>4</sub> /TiO <sub>2</sub>	CO <sub>2</sub> and H <sub>2</sub> O	8 W UV-light lamp	56.2 $\mu$ molh <sup>-1</sup> g <sup>-1</sup> CO	[177]	

Table 1. Cont.

Application	Photocatalyst	Photocatalysts Target	Source of Light	Efficiency	Ref.
Sterilization	CeO <sub>2</sub> /polymeric CN	<i>Staphylococcus aureus</i>	visible-light irradiation ( $\lambda \geq 420$ nm)	88% sterilization	[129]
	$\alpha$ -Fe <sub>2</sub> O <sub>3</sub> /g-C <sub>3</sub> N <sub>4</sub>	<i>Escherichia coli</i>	300 W Xenon lamp, 400 nm ultraviolet cut-off filter	>80% sterilization	[178]
	P-doped MoS <sub>2</sub> /g-C <sub>3</sub> N <sub>4</sub>	<i>Escherichia coli</i>	Visible light	100% sterilization	[179]
	Sn <sub>3</sub> O <sub>4</sub> /PTCDI	<i>Staphylococcus aureus</i> and <i>Escherichia coli</i>	Simulated sunlight	>90% sterilization	[180]
Reduction of heavy metals	TiO <sub>2</sub> /WO <sub>3</sub> /PANI	Cr(VI) 10 mgL <sup>-1</sup>	400 W visible lamp (2600 Lux)	68%	[181]
	PVP/Bi <sub>2</sub> S <sub>3</sub>	Cr(VI) 10 mgL <sup>-1</sup>	Visible light	95%	[182]
	PW <sub>12</sub> /CN/Bi <sub>2</sub> WO <sub>6</sub>	Cr(VI) 20 mgL <sup>-1</sup>	1KW xenon lamp ( $\lambda > 420$ nm)	98%	[183]

### 6.1. Environmental Applications: Pollutants Degradation, Reduction of Heavy Metals, Sterilization

In the field of the degradation of pollutants, Han et al. [161] describe how the  $\pi$ - $\pi$  stacking in perylene imide/Bi<sub>2</sub>WO<sub>6</sub> hybrid photocatalyst enhances the photocatalytic activity for the degradation of Bisphenol A (BPA), also underlining the good stability and recyclability. The 2D sheet-like structure observed in the SEM measurements promotes the presence of a high concentration of active sites on the surface. The presence of the polymer facilitates the separation of the charge carriers, increasing the photocatalytic activity joined to the nanosheet-like structure that increases the number of active sites for the reaction (Figure 11). The photocatalytic tests show that by increasing the percentage of Bi<sub>2</sub>WO<sub>3</sub> in the hybrid first, the photocatalytic activity increases and then decreases, and the best activity has been observed when 30% of Bi<sub>2</sub>WO<sub>3</sub> is present, and it is stable even after five cycles (Figure 12).

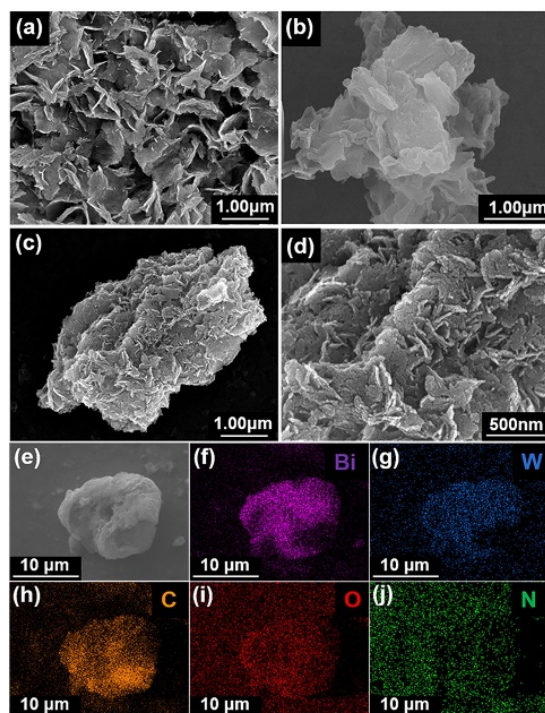
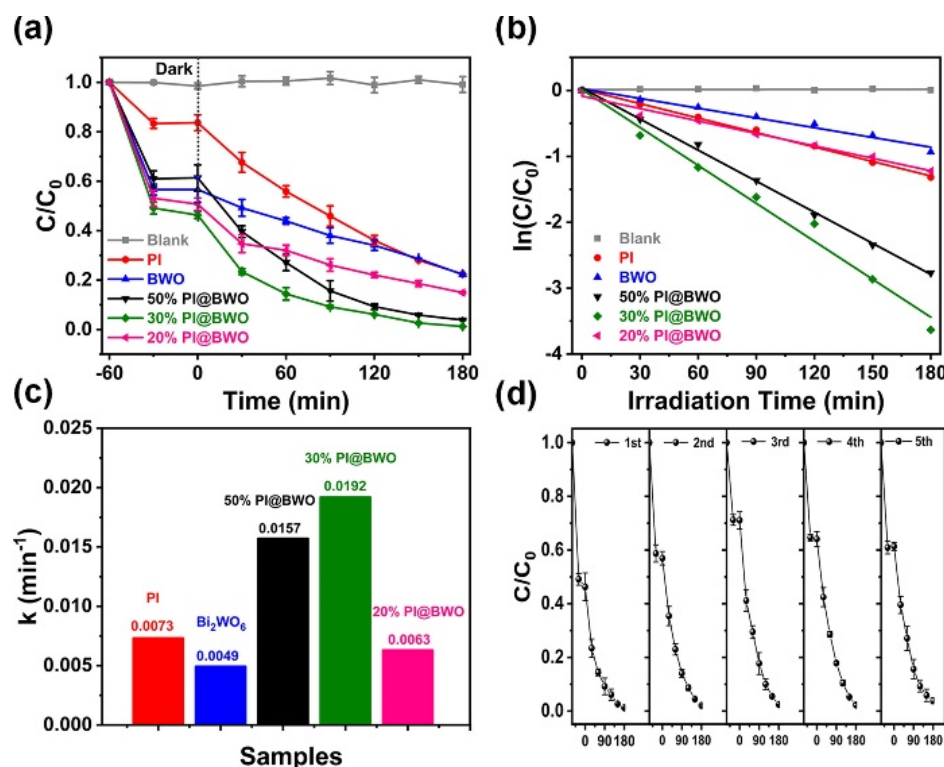


Figure 11. SEM images of (a) BWO nanosheets, (b) PI, (c,d) 30% PI@BWO and magnification, (e) FE-SEM images of 30% PI@BWO and (f–j) EDX element mapping images of Bi, W, C, O, and N.



**Figure 12.** (a) BPA photocatalytic removal performance over as-prepared samples under visible light illumination, (b) pseudo-first-order kinetics equation fitted with the BPA degradation processes over different samples, (c) kinetic rate constants ( $\text{min}^{-1}$ ) of the samples, (d) five consecutive photocatalytic degradation cycles over 30% PI@BWO [161].

The modifications through the modulation of the organic mesh represent a further strategy to increase the photocatalytic activity of the material. The introduction of phenyl rings in the mesh of  $g\text{-C}_3\text{N}_4$  was utilized to shift the absorption edge in the visible range and to obtain an efficient hybrid photocatalyst (Phenyl modified- $\text{TiO}_2$  hereafter PhCN) up to 600 nm (Figure 13) [96,166]. The absorption spectrum of the hybrid system appears as the sum of the two building blocks.

The phenyl-modified carbon nitride presents lower band gap LUMO levels almost resonant with the conduction band of  $\text{TiO}_2$ ; the electrons are promoted from the HOMO ground state into the LUMO excited state of the phenyl carbon nitride and then transferred to the conduction band of the  $\text{TiO}_2$ . The degradation efficiency for Rhodamine B and Methylene Blue under white LED irradiation increased from 4% by using pure compounds to 17% by using only  $g\text{-C}_3\text{N}_4/\text{TiO}_2$ , raising to 98% and 88% with the hybrid system PhCN/ $\text{TiO}_2$  (Figure 14).

New methods for killing antibiotic-resistant bacteria have gained large interest in the last year, and in this field, photocatalysis is widely used. The hybrid photocatalyst studied by Yang et al. [180] appears to be very efficient in capturing bacteria. TEM images of the  $\text{Sn}_3\text{O}_4/\text{PDINH}$  hybrid show an organic amorphous layer with a thickness of about 5nm on the surface of  $\text{Sn}_3\text{O}_4$  nanosheets. The formation of the composite has been further confirmed by EDS analysis, which reveals the presence of Sn, O, C, and N (Figure 15). This hybrid photocatalyst obtained by coupling  $\text{Sn}_3\text{O}_4$  and perylene diimide, thanks to the  $\pi\text{-}\pi$  bonding interactions, allows generating active oxygen species capable of killing the bacteria because these species interact with proteins, lipids, and other components of the bacteria, causing death. The photocatalytic antibacterial activity has been evaluated by performing the plate-counting method. The highest observed capture rate for this hybrid has been 82%, improved by the presence of the organic polymer on the surface (Figure 16).

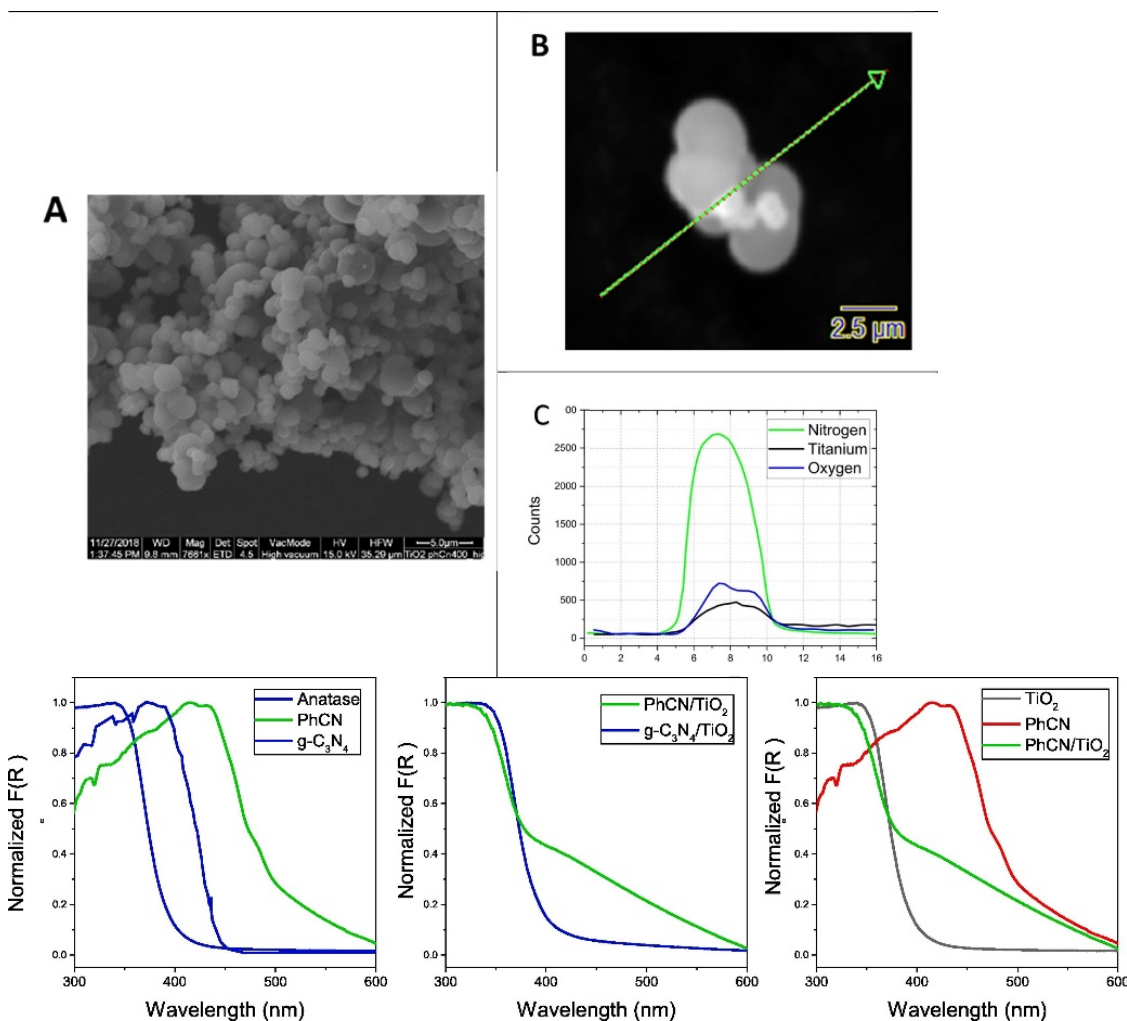


**Figure 13.** SEM images of PhCN/TiO<sub>2</sub> hybrid system taken at low (A) and high magnification (B) and EDX analysis for the cross-section denoted by the dashed green. Normalized absorption spectra of TiO<sub>2</sub> (anatase), g-C<sub>3</sub>N<sub>4</sub>, and PhCN (i.e., the building blocks for the hybrid systems) (A), the hybrid systems g-C<sub>3</sub>N<sub>4</sub>/TiO<sub>2</sub> and PhCN/TiO<sub>2</sub> (B), and the differential absorption of PhCN/TiO<sub>2</sub> from building blocks (C) [166].

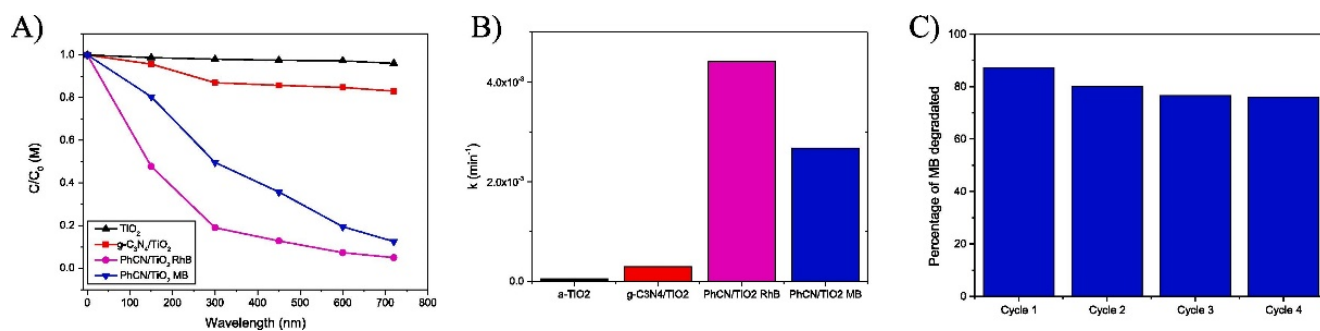


**Figure 14.** PhCN/TiO<sub>2</sub> photocatalyst and its application for the degradation of RhB and MB (A). Rate constant (*k*) by employing TiO<sub>2</sub> (anatase), g-C<sub>3</sub>N<sub>4</sub>/TiO<sub>2</sub>, and PhCN/TiO<sub>2</sub> as photocatalysts respectively (B). The stability of the catalyst is reported for the MB photodegradation (C) [166].

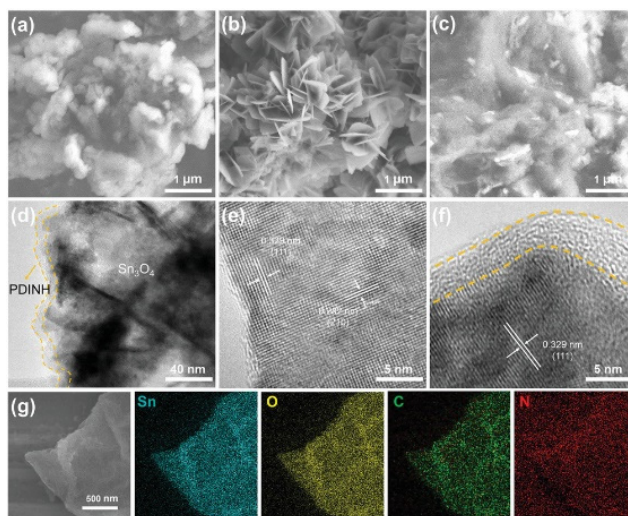


**Figure 15.** SEM images of (a) PDINH, (b) Sn<sub>3</sub>O<sub>4</sub>, and (c) Sn<sub>3</sub>O<sub>4</sub>/PDINH–10%. (d) TEM image of Sn<sub>3</sub>O<sub>4</sub>/PDINH–10%. HRTEM images of (e) Sn<sub>3</sub>O<sub>4</sub> and (f) Sn<sub>3</sub>O<sub>4</sub> /PDINH-10%. (g) EDS element mapping of Sn<sub>3</sub>O<sub>4</sub>/PDINH–10%.

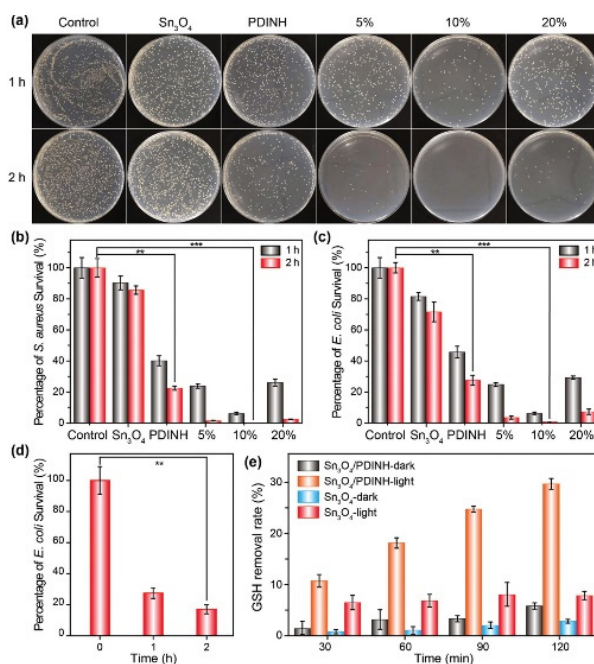


**Figure 16.** Antibacterial activity. (a) Photographs of antibacterial results under simulated sunlight illumination (*S. aureus*). Antibacterial activities of the different materials under simulated sunlight illumination: (b) *S. aureus* and (c) *E. coli*. (d) Antibacterial performance of Sn<sub>3</sub>O<sub>4</sub>/PDINH heterostructure under NIR irradiation ( $\lambda > 700$  nm). (e) GSH losing histograms after incubation with materials under simulated sunlight illumination or not [180].

Shen et al. synthesized novel three-dimensional Bi<sub>2</sub>S<sub>3</sub> nanocrystals capped by polyvinyl pyrrolidone photocatalyst for the reduction of hexavalent chromium under visible light irradiation. TEM images display flower-like structures consisting of nanosheets (Figure 17). The reduction of metals with such an impressive photocatalyst reaches 95% in only 5 min of reaction (Figure 18).

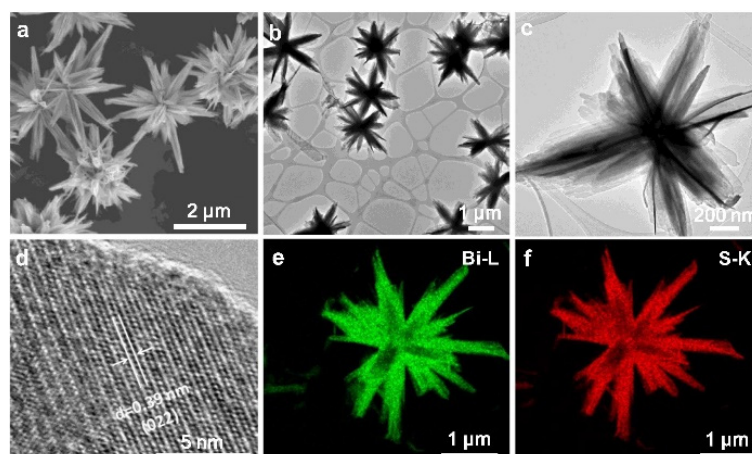


**Figure 17.** (a) SEM and (b,c) TEM images with different magnifications of  $\text{Bi}_2\text{S}_3-1$ . (d) HRTEM image and (e,f) EDS elemental mapping of  $\text{Bi}_2\text{S}_3-1$ .

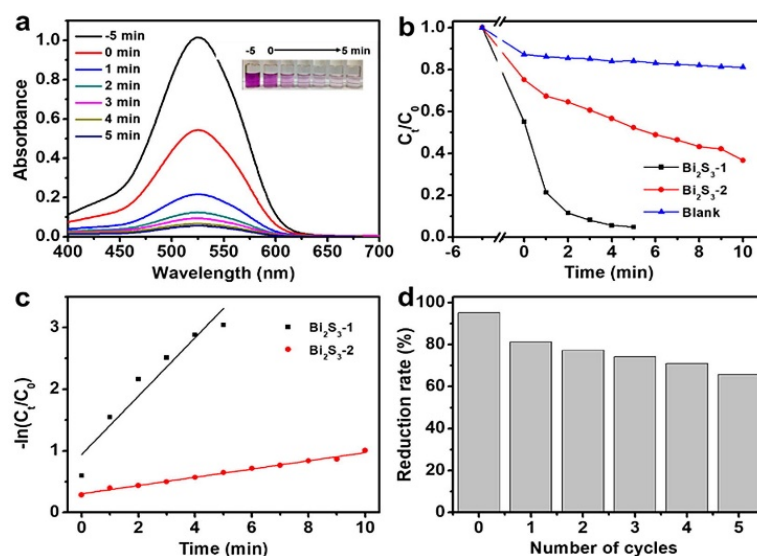


**Figure 18.** (a) Absorption spectra of RhB solution at different times of photodegradation with  $\text{Bi}_2\text{S}_3-1$  (the inset in the right corner is an image of RhB solution before and after photodegradation). (b) Variation of RhB concentration with photodegradation time in the existence of various photocatalysts ( $\text{Bi}_2\text{S}_3-1$ ,  $\text{Bi}_2\text{S}_3-2$ , and  $\text{TiO}_2$ ) under visible light. (c)  $-\ln(C_t/C_0)$  versus time curves of  $\text{Bi}_2\text{S}_3-1$ ,  $\text{Bi}_2\text{S}_3-2$  and  $\text{TiO}_2$ . (d) The durability tests of  $\text{Bi}_2\text{S}_3-1$  for photodegradation of RhB [182].

## 6.2. Energy: $\text{CO}_2$ Reduction and $\text{H}_2$ Evolution

The formation of two-dimensional (2D) nanostructures of the polymeric structure is a successful strategy to increase the photocatalytic activity: higher aspect ratio, larger surface area, and increased number of surface groups for anchoring cocatalysts are fundamental properties of the layered structures. Two-dimensional  $g\text{-C}_3\text{N}_4$  nanosheets have been successfully obtained, and significantly photocatalytic performance was reported [97,133].

For  $\text{CO}_2$  reduction, a new and very stable 0D/2D hybrid system has been proposed by Gong et al. [173]. This photocatalyst, with a high surface area, presents high photocatalytic activity because of the presence of a large number of active sites. In SEM images, the hybrids systems show the nanosheet structure and no adhesive nanoparticles on the surface (Figure 19). The observed reduction rate for the  $\text{CO}_2$  reduction has been  $69.8 \mu\text{mol g}^{-1} \text{g}^{-1}$  under visible light irradiation (Figure 20).

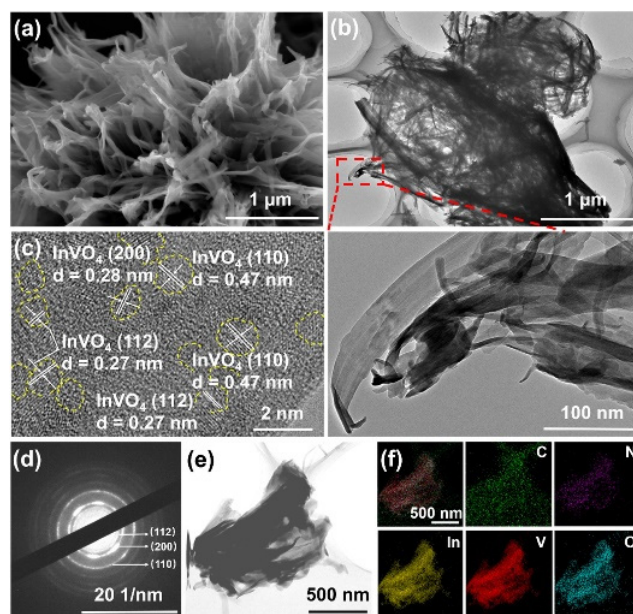


**Figure 19.** SEM image (a), TEM images (b), HRTEM image (c), SAED pattern (d), HAADF–STEM image (e) and corresponding EDX elemental mapping images (f) of  $\text{InVO}_4/\text{CN-II}$ .

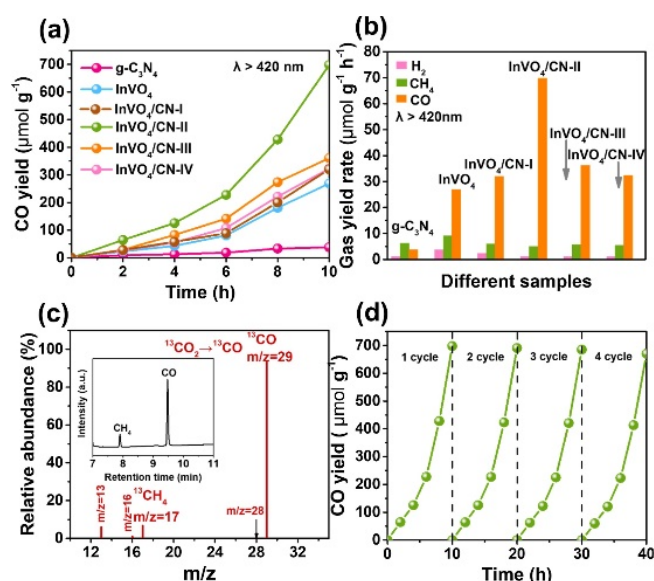


**Figure 20.** (a) CO generation and (b) average gas evolution rates of  $\text{H}_2$ ,  $\text{CH}_4$ , and  $\text{CO}$  in  $\text{MeCN}/\text{H}_2\text{O}$  system over various photocatalysts for 10 h photocatalytic reaction under visible light irradiation (with a UVCUT–420 nm filter). (c) Mass spectrum of  $^{13}\text{CO}$  ( $m/z = 29$ ) produced over  $\text{InVO}_4/\text{CN-II}$  in the photoreduction of  $^{13}\text{CO}_2$ . (d) Cycling production of  $\text{CO}$  over  $\text{InVO}_4/\text{CN-II}$  under visible light irradiation [173].

The production of  $\text{H}_2$  as an energy source has been studied increasingly in the last few years. Hamdy et al. [168] propose a novel polyaniline/ $\text{ZnO}$  heterojunction, synthesized via sol-gel/polymerization route for photocatalytic hydrogen production under a visible light source.

The amount of polymer has a fundamental role in photocatalytic activity as it plays a uniform deposition of it on the  $\text{ZnO}$  surface (Figure 21).

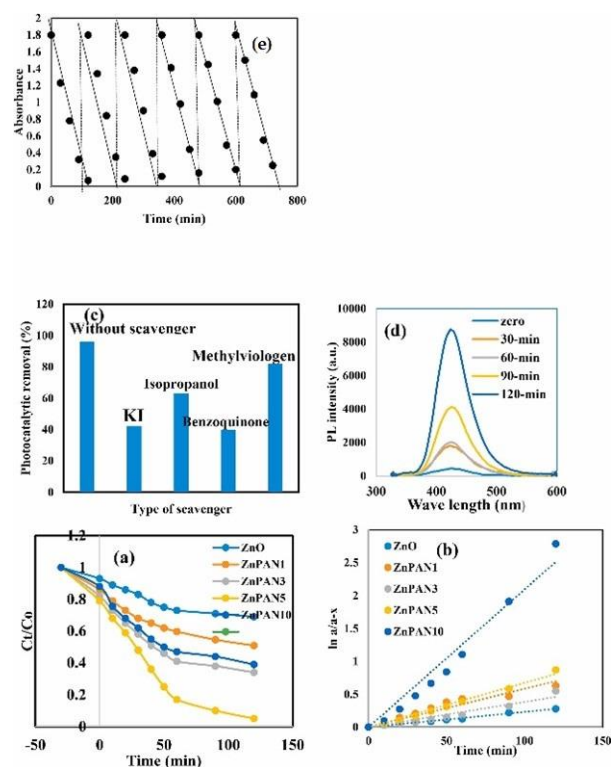


**Figure 21.** (a) Photocatalytic degradation of FLU dye over ZnO, ZnPAN1, ZnPAN3, ZnPAN5, and ZnPAN10, (b) Pseudo-first order kinetic for photodegradation of FLU dye over ZnO, ZnPAN1, ZnPAN3, ZnPAN5 and ZnPAN10, (c) The effect of scavengers on photocatalytic degradation of FLU dye over ZnPAN5, (d) PL spectrum for terephthalic acid on the sample ZnPAN5 (e) Re-cyclic of ZnPAN5 for five consecutive cycles [168].

Zang et al. showed how the p-conjugation, the flexibility, and the high surface area of pyrene-based polymer coupled with MoS<sub>2</sub> enhance photocatalytic H<sub>2</sub> production [170]. Under visible light irradiation, the electrons can be quickly transferred from the conduction band of pyrene-based polymer to MoS<sub>2</sub> restraining the charge recombination process (Figure 22).

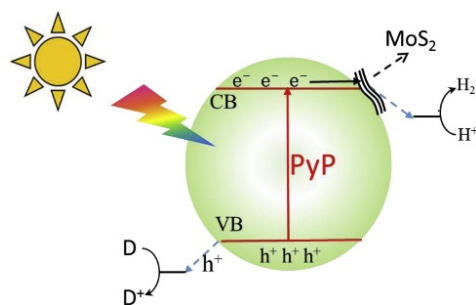


**Figure 22.** Schematic illustration of the between PyP and MoS<sub>2</sub>. D = donor [170].

From SEM and TEM measurements, it is possible to observe the different morphology of the two components of the hybrid system. The PyP particle size is 40–100 nm while MoS<sub>2</sub> shows a nanosheet-like structure with few nanometers of thickness, as it is well distinguishable in the TEM images (Figure 23). The photocatalytic activity is enhanced by the fast transfer of the excited electrons from the conduction band of the PyP to the MoS<sub>2</sub>, whose surface is covered with active sites, allowing the photocatalytic process.

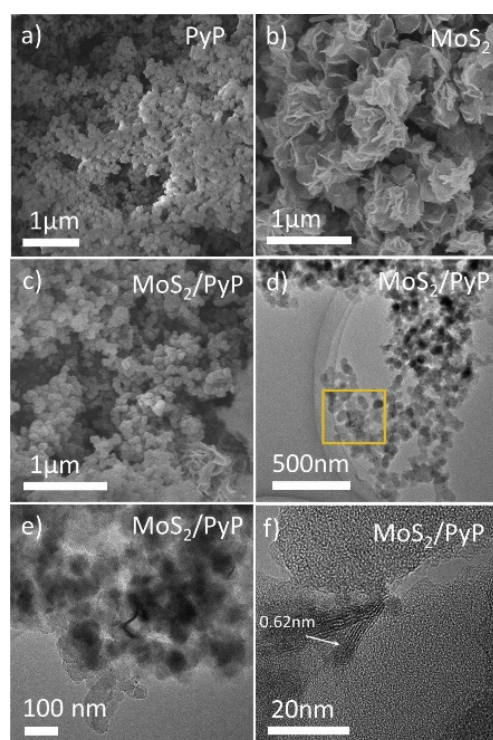


**Figure 23.** SEM images of (a) pure PyP, (b) MoS<sub>2</sub> (c) 3 wt. % MoS<sub>2</sub>/PyP(IM) samples; (d–f) TEM images of 3 wt. % MoS<sub>2</sub>/PyP(IM) samples.

Wang et al. designed TiO<sub>2</sub>-modified g-C<sub>3</sub>N<sub>4</sub> composite photocatalysts using the ball milling synthesis method followed by a calcination process. From spectroscopic measurements and morphological studies, they confirmed the formation of the heterostructure that reflects an enhancement of the separation rate of the photogenerated electrons and holes and, therefore, of the CO<sub>2</sub> reduction rate (Figure 24) [177].

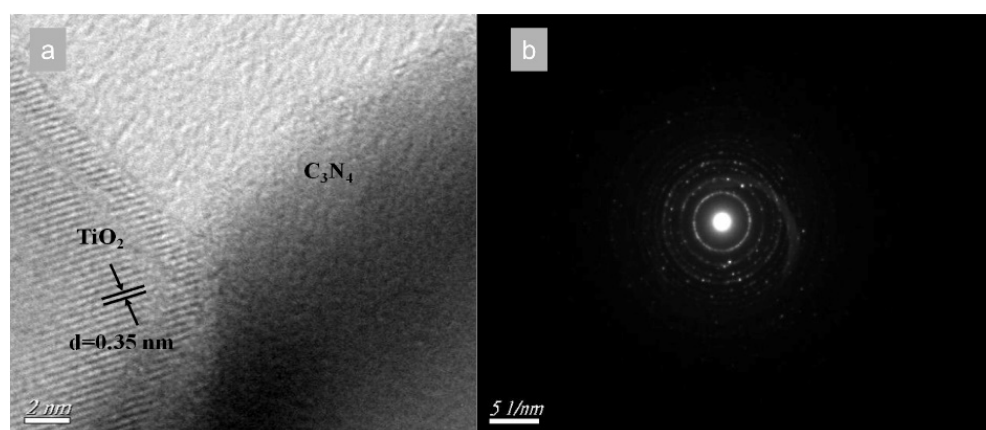


**Figure 24.** The HR-TEM image (a) and SAED pattern (b) of C<sub>3</sub>N<sub>4</sub>/TiO<sub>2</sub> composite photocatalysts [177].

From SEM analysis emerges an irregular structure with aggregates of bulk g-C<sub>3</sub>N<sub>4</sub> and TiO<sub>2</sub> nanoparticles with 20–50 nm size on its multilayered surface (Figure 25). The formation of the heterostructure promotes the separation between the electron and the holes, and the best photocatalytic result shows the yields of 72.2 and 56.2 μmol g<sup>-1</sup> for CH<sub>4</sub> and CO, respectively

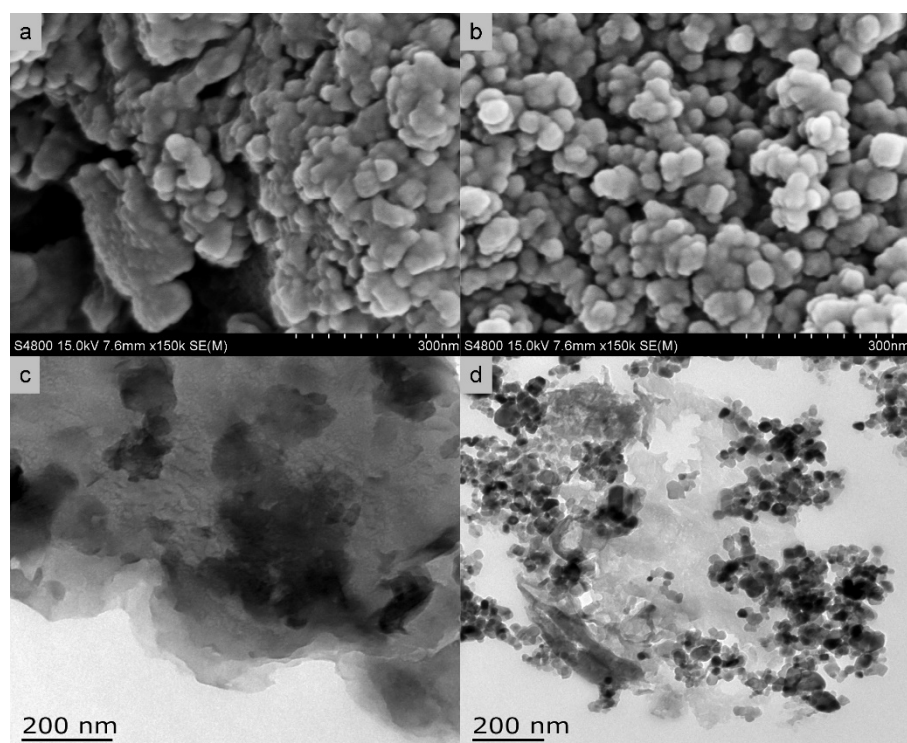


**Figure 25.** SEM (a,b) and TEM (c,d) images of as prepared photocatalysts: (a,c) pure bulk  $C_3N_4$ , (b,d)  $C_3N_4/TiO_2$  composite photocatalysts.

In summary, hybrid organic/inorganic photocatalysts have emerged as highly potential materials to drastically improve visible photocatalytic efficiency. Our review cannot be fully comprehensive for the large amount of new scientific products that are available daily, but it would represent a guide for readers that want to enter more insights into the field of photocatalysis. More specifically, we presented the high potential impact of the use of visible light for environmental remediation and energy production.

## 7. Conclusions and Outlook

“Set the controls for the heart of the sun”, sang Pink Floyd; we can now better paraphrase the title as “Set the control for the use of the heart of the sun”. The visible-driven photocatalytic process has become a rapid and important strategy to mitigate the anthropogenic impact and mitigate energy consumption. Even if different solutions have already been proposed and, in some cases, good performances have been achieved, the road is still long. Starting from the wide galaxy of the actual literature, it will be possible to set the control of the best parameters to use solar radiation in the photocatalytic properties.

In this review, we analyzed the state art inorganic and organic semiconductors underlining how the improvement of the absorption in the visible range represents a crucial point in the actual research and how the study of heterostructures can overcome this problem.

New Materials with reduced environmental impact, the use of hybrid solutions to overcome the limitations of pure inorganic and organic materials, surface modification, doping processes, and new heterostructures are important parameters to set the more appropriate energy level and recombination process.

The review aims to provide a useful guideline for designing and developing new photocatalysts useful to find suitable roads to achieve the use of the Heart of the Sun.

**Author Contributions:** Conceptualization, S.P., P.C.R. and F.S.; writing—original draft preparation, S.P. and P.C.R.; writing—review and editing, S.P. and P.C.R.; supervision, S.P., P.C.R. and F.S. All authors have read and agreed to the published version of the manuscript.

**Funding:** This work was supported by the “Fondazione di Sardegna” within the project F75F21001230007 “Paint4Vid—Visible photocatalytic materials for viruses and bacteria inactivation”.

**Conflicts of Interest:** The authors declare no conflict of interest.

## References

1. Manisalidis, I.; Stavropoulou, E.; Stavropoulos, A.; Bezirtzoglou, E. Environmental and Health Impacts of Air Pollution: A Review. *Front. Public Health* **2020**, *8*, 14. [[CrossRef](#)] [[PubMed](#)]
2. Delbeke, J.; Runge-Metzger, A.; Slingenberg, Y.; Werksman, J. The paris agreement. *Towards A Clim.-Neutral Eur. Curbing Trend* **2019**, *22*, 24–45. [[CrossRef](#)]
3. Yadav, S.; Shakya, K.; Gupta, A.; Singh, D.; Chandran, A.R.; Aanappalli, A.V.; Goyal, K.; Rani, N.; Saini, K. A review on degradation of organic dyes by using metal oxide semiconductors. *Environ. Sci. Pollut. Res.* **2022**. [[CrossRef](#)] [[PubMed](#)]
4. Shindhal, T.; Rakholiya, P.; Varjani, S.; Pandey, A.; Ngo, H.H.; Guo, W.; Ng, H.Y.; Taherzadeh, M.J. A critical review on advances in the practices and perspectives for the treatment of dye industry wastewater. *Bioengineered* **2021**, *12*, 70–87. [[CrossRef](#)] [[PubMed](#)]
5. Zhong, N.; Yuan, J.; Luo, Y.; Zhao, M.; Luo, B.; Liao, Q.; Chang, H.; Zhong, D.; Rittmann, B.E. Intimately coupling photocatalysis with phenolics biodegradation and photosynthesis. *Chem. Eng. J.* **2021**, *425*, 130666. [[CrossRef](#)]
6. Yadav, G.; Ahmaruzzaman, M. New generation advanced nanomaterials for photocatalytic abatement of phenolic compounds. *Chemosphere* **2022**, *304*, 135297. [[CrossRef](#)] [[PubMed](#)]
7. Lotfi, H.; Heydarinasab, A.; Mansouri, M.; Hosseini, S.H. Kinetic modeling of removal of aromatic hydrocarbons from petroleum wastewaters by UiO-66-NH<sub>2</sub>/TiO<sub>2</sub>/ZnO nanocomposite. *J. Environ. Chem. Eng.* **2022**, *10*, 107066. [[CrossRef](#)]
8. Pica, M. Treatment of wastewaters with zirconium phosphate based materials: A review on efficient systems for the removal of heavy metal and dye water pollutants. *Molecules* **2021**, *26*, 2392. [[CrossRef](#)] [[PubMed](#)]
9. Qasem, N.A.A.; Mohammed, R.H.; Lawal, D.U. Removal of heavy metal ions from wastewater: A comprehensive and critical review. *Npj Clean Water* **2021**, *4*, 36. [[CrossRef](#)]
10. Nguyen, D.N.; Bui, H.M.; Nguyen, H.Q. *Heterogeneous Photocatalysis for the Removal of Pharmaceutical Compounds*; Elsevier B.V.: Amsterdam, The Netherlands, 2020; ISBN 9780128195949.
11. Yang, X.; Chen, Z.; Zhao, W.; Liu, C.; Qian, X.; Zhang, M.; Wei, G.; Khan, E.; Hau Ng, Y.; Sik Ok, Y. Recent advances in photodegradation of antibiotic residues in water. *Chem. Eng. J.* **2021**, *405*, 126806. [[CrossRef](#)]
12. Fujishima, A.; Honda, K. Electrochemical Photolysis of Water at a Semiconductor Electrode. *Nature* **1972**, *238*, 37–38. [[CrossRef](#)] [[PubMed](#)]
13. Fernandes, S.; de Silva, J.C.Q.E.; da Silva, L.P. Life Cycle Assessment of the Sustainability of Enhancing the Photodegradation Activity of TiO<sub>2</sub> with Metal-Doping. *Materials* **2020**, *13*, 1487. [[CrossRef](#)] [[PubMed](#)]
14. Fernández-ibáñez, P. Solar-driven Photocatalyzed Hydrogen Production from Water cleavage: Evaluation and Process Life Cycle Assessment. *J. Phys. Conf. Ser.* **2022**, *2305*, 012040. [[CrossRef](#)]
15. Wang, H.; Li, X.; Zhao, X.; Li, C.; Song, X.; Zhang, P.; Huo, P. A review on heterogeneous photocatalysis for environmental remediation: From semiconductors to modification strategies. *Chin. J. Catal.* **2022**, *43*, 178–214. [[CrossRef](#)]
16. Kumar, A.; Choudhary, P.; Kumar, A.; Camargo, P.H.C.; Krishnan, V. Recent Advances in Plasmonic Photocatalysis Based on TiO<sub>2</sub> and Noble Metal Nanoparticles for Energy Conversion, Environmental Remediation, and Organic Synthesis. *Small* **2022**, *18*, e2101638. [[CrossRef](#)]
17. Candish, L.; Collins, K.D.; Cook, G.C.; Douglas, J.J.; Gómez-Suárez, A.; Jolit, A.; Keess, S. Photocatalysis in the Life Science Industry. *Chem. Rev.* **2022**, *122*, 2907–2980. [[CrossRef](#)] [[PubMed](#)]
18. Nakata, K.; Fujishima, A. TiO<sub>2</sub> photocatalysis: Design and applications. *J. Photochem. Photobiol. C Photochem. Rev.* **2012**, *13*, 169–189. [[CrossRef](#)]
19. Yao, G.; Liu, Y.; Liu, J.; Xu, Y. Facile Synthesis of Porous g-C<sub>3</sub>N<sub>4</sub> with Enhanced Visible-Light Photoactivity. *Molecules* **2022**, *27*, 1754. [[CrossRef](#)]
20. Shah, S.A.; Khan, I.; Yuan, A. MoS<sub>2</sub> as a Co-Catalyst for Photocatalytic Hydrogen Production: A Mini Review. *Molecules* **2022**, *27*, 3289. [[CrossRef](#)]
21. Hai, G.; Wang, H. Theoretical studies of metal-organic frameworks: Calculation methods and applications in catalysis, gas separation, and energy storage. *Coord. Chem. Rev.* **2022**, *469*, 214670. [[CrossRef](#)]
22. Swain, S.; Altaee, A.; Saxena, M.; Samal, A.K. A comprehensive study on heterogeneous single atom catalysis: Current progress, and challenges q. *Coord. Chem. Rev.* **2022**, *470*, 214710. [[CrossRef](#)]
23. Bomeriame, H.; Da Silva, E.S.; Cherevan, A.S.; Chafik, T.; Faria, J.L.; Eder, D. Layered double hydroxide (LDH)-based materials: A mini-review on strategies to improve the performance for photocatalytic water splitting. *J. Energy Chem.* **2021**, *64*, 406–431. [[CrossRef](#)]
24. Zhao, J.; Ren, J.; Zhang, G.; Zhao, Z.; Liu, S.; Zhang, W.; Chen, L. Donor-Acceptor Type Covalent Organic Frameworks. *Chem. Eur. J.* **2021**, *27*, 10781–107977. [[CrossRef](#)]
25. Chen, J.; Abazari, R.; Adegoke, K.A.; Maxakato, N.W.; Bello, O.S.; Tahir, M.; Tasleem, S.; Sanati, S.; Kirillov, A.M.; Zhou, Y. Metal-organic frameworks and derived materials as photocatalysts for water splitting and carbon dioxide reduction. *Coord. Chem. Rev.* **2022**, *469*, 214664. [[CrossRef](#)]

26. Zhou, Y.; Lu, F.; Fang, T.; Gu, D.; Feng, X.; Song, T.; Liu, W. A brief review on metal halide perovskite photocatalysts: History, applications and prospects. *J. Alloys Compd.* **2022**, *911*, 165062. [[CrossRef](#)]
27. Al-Azri, Z.H.N.; Aloufi, M.; Chan, A.; Waterhouse, G.I.N.; Idriss, H. Metal Particle Size Effects on the Photocatalytic Hydrogen Ion Reduction. *ACS Catal.* **2019**, *9*, 3946–3958. [[CrossRef](#)]
28. Kuznetsov, A.E. Review of research of nanocomposites based on graphene quantum dots. *Comput. Chem. Appl. New Technol.* **2021**, 135–160. [[CrossRef](#)]
29. Humayun, M.; Wang, C.; Luo, W. Recent Progress in the Synthesis and Applications of Composite Photocatalysts: A Critical Review. *Small Methods* **2022**, *6*, 2101395. [[CrossRef](#)]
30. Wang, C.Y.; Maeda, K.; Chang, L.L.; Tung, K.L.; Hu, C. Synthesis and applications of carbon nitride (CN<sub>x</sub>) family with different carbon to nitrogen ratio. *Carbon* **2022**, *188*, 482–491. [[CrossRef](#)]
31. Jedla, M.R.; Koneru, B.; Franco, A.; Rangappa, D.; Banerjee, P. Recent developments in nanomaterials based adsorbents for water purification techniques. *Biointerface Res. Appl. Chem.* **2022**, *12*, 5821–5835. [[CrossRef](#)]
32. Almaie, S.; Vatanpour, V.; Hossein, M. Chemosphere Volatile organic compounds (VOCs) removal by photocatalysts: A review. *Chemosphere* **2022**, *306*, 135655. [[CrossRef](#)]
33. Castilla-Caballero, D.; Sadak, O.; Martínez-Díaz, J.; Martínez-Castro, V.; Colina-Márquez, J.; Machuca-Martínez, F.; Hernandez-Ramirez, A.; Vazquez-Rodriguez, S.; Gunasekaran, S. Solid-state photocatalysis for plastics abatement: A review. *Mater. Sci. Semicond. Process.* **2022**, *149*, 106890. [[CrossRef](#)]
34. Hazaraimi, M.H.; Goh, P.S.; Lau, W.J.; Ismail, A.F.; Wu, Z.; Subramaniam, M.N.; Lim, J.W.; Kanakaraju, D. The state-of-the-art development of photocatalysts for degrading of persistent herbicides in aqueous environment. *Sci. Total Environ.* **2022**, *843*, 156975. [[CrossRef](#)]
35. Wang, Y.; Torres, J.A.; Shviro, M.; Carmo, M.; He, T.; Ribeiro, C. Photocatalytic materials applications for sustainable agriculture. *Prog. Mater. Sci.* **2022**, *130*, 100965. [[CrossRef](#)]
36. Rajeshwar, K.; Osugi, M.E.; Chanmanee, W.; Chenthamarakshan, C.R.; Zaroni, M.V.B.; Kajitvichyanukul, P.; Krishnan-Ayer, R. Heterogeneous photocatalytic treatment of organic dyes in air and aqueous media. *J. Photochem. Photobiol. C Photochem. Rev.* **2008**, *9*, 171–192. [[CrossRef](#)]
37. Rehman, S.; Ullah, R.; Butt, A.M.; Gohar, N.D. Strategies of making TiO<sub>2</sub> and ZnO visible light active. *J. Hazard. Mater.* **2009**, *170*, 560–569. [[CrossRef](#)]
38. Aslam, M.; Fazal, D.B.; Ahmad, F.; Fazal, A.B.; Abdullah, A.Z.; Ahmed, M.; Qamar, M.; Rafatullah, M. Photocatalytic Degradation of Recalcitrant Pollutants of Greywater. *Catalysts* **2022**, *12*, 557. [[CrossRef](#)]
39. Ren, Y.; Yu, C.; Tan, X.; Wei, Q.; Wang, Z.; Ni, L.; Wang, L.; Qiu, J. Strategies to activate inert nitrogen molecules for efficient ammonia electrosynthesis: Current status, challenges, and perspectives. *Energy Environ. Sci.* **2022**, *15*, 2776–2805. [[CrossRef](#)]
40. Saravanan, R.; Gracia, F.; Stephen, A. Basic Principles, Mechanism, and Challenges of Photocatalysis. In *Nanocomposites for Visible Light-Induced Photocatalysis*; Springer Series on Polymer and Composite Materials; Khan, M., Pradhan, D., Sohn, Y., Eds.; Springer: Berlin, Germany, 2017; pp. 19–40.
41. Cernuto, G.; Masciocchi, N.; Cervellino, A.; Colonna, G.M.; Guagliardi, A. Size and shape dependence of the photocatalytic activity of TiO<sub>2</sub> nanocrystals: A total scattering Debye function study. *J. Am. Chem. Soc.* **2011**, *133*, 3114–3119. [[CrossRef](#)] [[PubMed](#)]
42. Zhang, M.; Salvador, P.A.; Rohrer, G.S. Influence of particle size and shape on the rate of hydrogen produced by Al-doped SrTiO<sub>3</sub> photocatalysts. *J. Am. Ceram. Soc.* **2022**, *108*, 5336–5346. [[CrossRef](#)]
43. Leng, D.; Wang, T.; Du, C.; Pei, X.; Wan, Y.; Wang, J. Synthesis of β-Bi<sub>2</sub>O<sub>3</sub> nanoparticles via the oxidation of Bi nanoparticles: Size, shape and polymorph control, anisotropic thermal expansion, and visible-light photocatalytic activity. *Ceram. Int.* **2022**, *48*, 18270–18277. [[CrossRef](#)]
44. Zheng, Y.; Duan, Z.; Liang, R.; Lv, R.; Wang, C.; Zhang, Z.; Wan, S.; Wang, S.; Xiong, H.; Ngaw, C.K.; et al. Shape-Dependent Performance of Cu/Cu<sub>2</sub>O for Photocatalytic Reduction of CO<sub>2</sub>. *ChemSusChem* **2022**, *15*, e202200216. [[CrossRef](#)]
45. Khan, M.M.; Adil, S.F.; Al-Mayouf, A. Metal oxides as photocatalysts. *J. Saudi Chem. Soc.* **2015**, *19*, 462–464. [[CrossRef](#)]
46. Saravanan, R.; Gupta, V.K.; Narayanan, V.; Stephen, A. Comparative study on photocatalytic activity of ZnO prepared by different methods. *J. Mol. Liq.* **2013**, *181*, 133–141. [[CrossRef](#)]
47. He, X.; Yang, Y.; Li, Y.; Chen, J.; Yang, S.; Liu, R.; Xu, Z. Effects of structure and surface properties on the performance of ZnO towards photocatalytic degradation of methylene blue. *Appl. Surf. Sci.* **2022**, *599*, 153898. [[CrossRef](#)]
48. Chatterjee, D.; Dasgupta, S. Visible light induced photocatalytic degradation of organic pollutants. *J. Photochem. Photobiol. C Photochem. Rev.* **2005**, *6*, 186–205. [[CrossRef](#)]
49. Castillo-Ledezma, J.H.; Salas, J.L.S.; López-Malo, A.; Bandala, E.R. Effect of pH, solar irradiation, and semiconductor concentration on the photocatalytic disinfection of Escherichia coli in water using nitrogen-doped TiO<sub>2</sub>. *Eur. Food Res. Technol.* **2011**, *233*, 825–834. [[CrossRef](#)]
50. Abbasi, S.; Hasanpour, M. The effect of pH on the photocatalytic degradation of methyl orange using decorated ZnO nanoparticles with SnO<sub>2</sub> nanoparticles. *J. Mater. Sci. Mater. Electron.* **2017**, *28*, 1307–1314. [[CrossRef](#)]
51. Reza, K.M.; Kurny, A.; Gulshan, F. Parameters affecting the photocatalytic degradation of dyes using TiO<sub>2</sub>: A review. *Appl. Water Sci.* **2017**, *7*, 1569–1578. [[CrossRef](#)]

52. Malato, S.; Fernández-Ibáñez, P.; Maldonado, M.I.; Blanco, J.; Gernjak, W. Decontamination and disinfection of water by solar photocatalysis: Recent overview and trends. *Catal. Today* **2009**, *147*, 1–59. [[CrossRef](#)]
53. Chen, L.-I.; Zhai, B.-g.; Huang, Y.M. Rendering Visible-Light Photocatalytic Activity to Undoped ZnO via Intrinsic Defects. *Eng. Catal.* **2020**, *10*, 1163. [[CrossRef](#)]
54. Zhou, H.; Qu, Y.; Zeid, T.; Duan, X. Towards highly efficient photocatalysts using semiconductor nanoarchitectures. *Energy Environ. Sci.* **2012**, *5*, 6732–6743. [[CrossRef](#)]
55. Solarska, R.; Królikowska, A.; Augustyński, J. Silver Nanoparticle Induced Photocurrent Enhancement at WO<sub>3</sub> Photoanodes. *Angew. Chem. Int. Ed.* **2010**, *49*, 7980–7983. [[CrossRef](#)] [[PubMed](#)]
56. Palmas, S.; Castresana, P.A.; Mais, L.; Vacca, A.; Mascia, M.; Ricci, P.C. TiO<sub>2</sub>-WO<sub>3</sub> nanostructured systems for photoelectrochemical applications. *RSC Adv.* **2016**, *6*, 101671–101682. [[CrossRef](#)]
57. Kay, A.; Cesar, I.; Grätzel, M. New benchmark for water photooxidation by nanostructured  $\alpha$ -Fe<sub>2</sub>O<sub>3</sub> films. *J. Am. Chem. Soc.* **2006**, *128*, 15714–15721. [[CrossRef](#)]
58. Ma, D.; Li, J.; Liu, A.; Chen, C. Carbon Gels-Modified TiO<sub>2</sub>: Promising Materials for Photocatalysis Applications. *Materials* **2020**, *13*, 1734. [[CrossRef](#)]
59. Frank, S.N.; Bard, A.J. Heterogeneous Photocatalytic Oxidation of Cyanide Ion in Aqueous Solutions at TiO<sub>2</sub> Powder. *J. Am. Chem. Soc.* **1977**, *99*, 303–304. [[CrossRef](#)]
60. Li, Y.; Ren, Z.; Gu, M.; Duan, Y.; Zhang, W.; Lv, K. Applied Catalysis B: Environmental Synergistic effect of interstitial C doping and oxygen vacancies on the photoreactivity of TiO<sub>2</sub> nanofibers towards CO<sub>2</sub> reduction. *Appl. Catal. B Environ.* **2022**, *317*, 121773. [[CrossRef](#)]
61. Nor, N.U.M.; Mazalan, E.; Risko, C.; Crocker, M.; Amin, N.A.S. Unveiling the structural, electronic, and optical effects of carbon-doping on multi-layer anatase TiO<sub>2</sub> (1 0 1) and the impact on photocatalysis. *Appl. Surf. Sci.* **2022**, *586*, 152641. [[CrossRef](#)]
62. Amor, C.O.; Elghniji, K.; Elaloui, E. Improving charge separation, photocurrent and photocatalytic activities of Dy-doped TiO<sub>2</sub> by surface modification with salicylic acid. *J. Mater. Sci. Mater. Electron.* **2020**, *31*, 20919–20931. [[CrossRef](#)]
63. Guetni, I.; Belaiche, M.; Ferdi, C.A.; Oulhakem, O.; Alaoui, K.B.; Naimi, Z. Engineering the photocatalytic efficiency of nanoscale TiO<sub>2</sub> anatase with doped (Nd/Y) and co-doped (Nd-Y/Nd-Sm) lanthanides to decompose the azo dye orange G under UV-VIS irradiation. *New J. Chem.* **2022**, *46*, 10162–10183. [[CrossRef](#)]
64. Khan, R.; Rahman, A.U. Band-Gap Narrowing of Titanium Dioxide by Nitrogen Doping. *Jpn. J. Appl. Phys.* **2001**, *40*, 561–563. [[CrossRef](#)]
65. Irie, H.; Watanabe, Y.; Hashimoto, K. Nitrogen-concentration dependence on photocatalytic activity of TiO<sub>2-x</sub>N<sub>x</sub> powders. *J. Phys. Chem. B* **2003**, *107*, 5483–5486. [[CrossRef](#)]
66. Ricci, P.C.; Casu, A.; Salis, M.; Corpino, R.; Anedda, A. Optically controlled phase variation of TiO<sub>2</sub> nanoparticles. *J. Phys. Chem. C* **2010**, *114*, 14441–14445. [[CrossRef](#)]
67. Chandrasekharan, N.; Kainat, P.Y. Improving the photoelectrochemical performance of nanostructured TiO<sub>2</sub> films by adsorption of gold nanoparticles. *J. Phys. Chem. B* **2000**, *104*, 10851–10857. [[CrossRef](#)]
68. Subramanian, V.; Wolf, E.E.; Kamat, P.V. Catalysis with TiO<sub>2</sub>/Gold Nanocomposites. Effect of Metal Particle Size on the Fermi Level Equilibration. *J. Am. Chem. Soc.* **2004**, *126*, 4943–4950. [[CrossRef](#)]
69. Wu, F.; Zhou, Z.; Hicks, A. Life Cycle Impact of Titanium Dioxide Nanoparticle Synthesis through Physical, Chemical, and Biological Routes. *Environ. Sci. Technol.* **2019**, *53*, 4078–4087. [[CrossRef](#)]
70. Lv, S.; Du, Y.; Wu, F.; Cai, Y.; Zhou, T. Review on LSPR assisted photocatalysis: Effects of physical fields and opportunities in multifield decoupling. *Nanoscale Adv.* **2022**, *4*, 2608–2631. [[CrossRef](#)]
71. Rycenga, M.; Cogley, C.M.; Zeng, J.; Li, W.; Moran, C.H.; Zhang, Q.; Qin, D.; Xia, Y. Controlling the synthesis and assembly of silver nanostructures for plasmonic applications. *Chem. Rev.* **2011**, *111*, 3669–3712. [[CrossRef](#)]
72. Aoki, Y.; Ishida, T.; Tatsuma, T. Plasmon-Induced Photocatalysis Based on Pt-Au Coupling with Enhanced Oxidation Abilities. *ACS Appl. Nano Mater.* **2022**, *5*, 4406–4412. [[CrossRef](#)]
73. Wang, H.; Wang, Y.; Guo, L.; Zhang, X.; Ribeiro, C.; He, T. Solar-heating boosted catalytic reduction of CO<sub>2</sub> under full-solar spectrum. *Chin. J. Catal.* **2020**, *41*, 131–139. [[CrossRef](#)]
74. Liu, T.; Besteiro, L.V.; Liedl, T.; Correa-Duarte, M.A.; Wang, Z.; Govorov, A.O. Chiral Plasmonic Nanocrystals for Generation of Hot Electrons: Toward Polarization-Sensitive Photochemistry. *Nano Lett.* **2019**, *19*, 1395–1407. [[CrossRef](#)]
75. Golze, S.D.; Porcu, S.; Zhu, C.; Sutter, E.; Ricci, P.C.; Kinzel, E.C.; Hughes, R.A.; Neretina, S. Sequential Symmetry-Breaking Events as a Synthetic Pathway for Chiral Gold Nanostructures with Spiral Geometries. *Nano Lett.* **2021**, *21*, 2919–2925. [[CrossRef](#)]
76. Dong, J.; Yan, C.; Chen, Y.; Zhou, W.; Peng, Y.; Zhang, Y.; Wang, L.N.; Huang, Z.H. Organic semiconductor nanostructures: Optoelectronic properties, modification strategies, and photocatalytic applications. *J. Mater. Sci. Technol.* **2022**, *113*, 175–198. [[CrossRef](#)]
77. Holmes, N.P.; Chambon, S.; Holmes, A.; Xu, X.; Hirakawa, K.; Deniau, E.; Lartigau-Dagron, C.; Bousquet, A. Organic semiconductor colloids: From the knowledge acquired in photovoltaics to the generation of solar hydrogen fuel. *Curr. Opin. Colloid Interface Sci.* **2021**, *56*, 101511. [[CrossRef](#)]
78. Viola, F.A.; Spanu, A.; Ricci, P.C.; Bonfiglio, A.; Cosseddu, P. Ultrathin, flexible and multimodal tactile sensors based on organic field-effect transistors. *Sci. Rep.* **2018**, *8*, 1–8. [[CrossRef](#)]

79. Cui, Y.; Yao, H.; Zhang, J.; Zhang, T.; Wang, Y.; Hong, L.; Xian, K.; Xu, B.; Zhang, S.; Peng, J.; et al. Over 16% efficiency organic photovoltaic cells enabled by a chlorinated acceptor with increased open-circuit voltages. *Nat. Commun.* **2019**, *10*, 2515. [CrossRef]
80. Mazzanti, M.; Milani, M.; Cristino, V.; Boaretto, R.; Molinari, A.; Caramori, S. Visible Light Reductive Photocatalysis of Azo-Dyes with n-n Junctions Based on Chemically Deposited CdS. *Molecules* **2022**, *27*, 2924. [CrossRef]
81. Fu, Z.; Wang, X.; Gardner, A.M.; Wang, X.; Chong, S.Y.; Neri, G.; Cowan, A.J.; Liu, L.; Li, X.; Vogel, A.; et al. A stable covalent organic framework for photocatalytic carbon dioxide reduction. *Chem. Sci.* **2020**, *11*, 543–550. [CrossRef]
82. Qian, Y.; Ma, D. Covalent organic frameworks: New materials platform for photocatalytic degradation of aqueous pollutants. *Materials* **2021**, *14*, 5600. [CrossRef]
83. Kroke, E.; Schwarz, M.; Horath-Bordon, E.; Kroll, P.; Noll, B.; Norman, A.D. Tri-s-triazine derivatives. Part I. From trichloro-tri-s-triazine to graphitic C<sub>3</sub>N<sub>4</sub> structures. *New J. Chem.* **2002**, *26*, 508–512. [CrossRef]
84. Li, Y.Y.; Ma, S.F.; Zhou, B.X.; Huang, W.Q.; Fan, X.; Li, X.; Li, K.; Huang, G.F. Hydroxy-carbonate-assisted synthesis of high porous graphitic carbon nitride with broken of hydrogen bonds as a highly efficient visible-light-driven photocatalyst. *J. Phys. D Appl. Phys.* **2019**, *52*, 105502. [CrossRef]
85. Li, Y.; Ruan, Z.; He, Y.; Li, J.; Li, K.; Jiang, Y.; Xu, X.; Yuan, Y.; Lin, K. In situ fabrication of hierarchically porous g-C<sub>3</sub>N<sub>4</sub> and understanding on its enhanced photocatalytic activity based on energy absorption. *Appl. Catal. B Environ.* **2018**, *236*, 64–75. [CrossRef]
86. Mousavi, M.; Habibi-Yangjeh, A.; Pouran, S.R. Review on magnetically separable graphitic carbon nitride-based nanocomposites as promising visible-light-driven photocatalysts. *J. Mater. Sci. Mater. Electron.* **2018**, *29*, 1719–1747. [CrossRef]
87. Vaya, D.; Kaushik, B.; Surolia, P.K. Recent advances in graphitic carbon nitride semiconductor: Structure, synthesis and applications. *Mater. Sci. Semicond. Process.* **2022**, *137*, 106181. [CrossRef]
88. Huang, D.; Li, Z.; Zeng, G.; Zhou, C.; Xue, W.; Gong, X.; Yan, X.; Chen, S.; Wang, W.; Cheng, M. Megamerger in photocatalytic field: 2D g-C<sub>3</sub>N<sub>4</sub> nanosheets serve as support of 0D nanomaterials for improving photocatalytic performance. *Appl. Catal. B Environ.* **2019**, *240*, 153–173. [CrossRef]
89. Zheng, Y.; Lin, L.; Wang, B.; Wang, X. Graphitic Carbon Nitride Polymers toward Sustainable Photoredox Catalysis. *Angew. Chem.-Int. Ed.* **2015**, *54*, 12868–12884. [CrossRef]
90. Ong, W.J.; Putri, L.K.; Tan, Y.C.; Tan, L.L.; Li, N.; Ng, Y.H.; Wen, X.; Chai, S.P. Unravelling charge carrier dynamics in protonated g-C<sub>3</sub>N<sub>4</sub> interfaced with carbon nanodots as co-catalysts toward enhanced photocatalytic CO<sub>2</sub> reduction: A combined experimental and first-principles DFT study. *Nano Res.* **2017**, *10*, 1673–1696. [CrossRef]
91. Cao, S.; Yu, J. G-C<sub>3</sub>N<sub>4</sub>-based photocatalysts for hydrogen generation. *J. Phys. Chem. Lett.* **2014**, *5*, 2101–2107. [CrossRef]
92. Dong, G.; Zhang, Y.; Pan, Q.; Qiu, J. A fantastic graphitic carbon nitride (g-C<sub>3</sub>N<sub>4</sub>) material: Electronic structure, photocatalytic and photoelectronic properties. *J. Photochem. Photobiol. C Photochem. Rev.* **2014**, *20*, 33–50. [CrossRef]
93. Liu, G.; Niu, P.; Sun, C.; Smith, S.C.; Chen, Z.; Lu, G.Q.; Cheng, H.M. Unique electronic structure induced high photoreactivity of sulfur-doped graphitic C<sub>3</sub>N<sub>4</sub>. *J. Am. Chem. Soc.* **2010**, *132*, 11642–11648. [CrossRef]
94. Hayat, A.; Sohail, M.; Ali Shah Syed, J.; Al-Sehemi, A.G.; Mohammed, M.H.; Al-Ghamdi, A.A.; Taha, T.A.; AlSalem, H.S.; Alenad, A.M.; Amin, M.A.; et al. Recent Advancement of the Current Aspects of g-C<sub>3</sub>N<sub>4</sub> for its Photocatalytic Applications in Sustainable Energy System. *Chem. Rec.* **2022**, *22*, e202100310. [CrossRef]
95. Zhang, Y.; Pan, Q.; Chai, G.; Liang, M.; Dong, G.; Zhang, Q.; Qiu, J. Synthesis and luminescence mechanism of multicolor-emitting g-C<sub>3</sub>N<sub>4</sub> nanopowders by low temperature thermal condensation of melamine. *Sci. Rep.* **2013**, *3*, 1943. [CrossRef]
96. Porcu, S.; Roppolo, I.; Salaun, M.; Sarais, G.; Barbarossa, S.; Casula, M.F.; Carbonaro, C.M.; Ricci, P.C. Come to light: Detailed analysis of thermally treated Phenyl modified Carbon Nitride Polymorphs for bright phosphors in lighting applications. *Appl. Surf. Sci.* **2020**, *504*, 144330. [CrossRef]
97. Porcu, S.; Secci, F.; Abdullah, Q.A.; Ricci, P.C. 4-Nitrophenol Efficient Photoreduction from Exfoliated and Protonated Phenyl-Doped Graphitic Carbon Nitride Nanosheets. *Polymers* **2021**, *13*, 3752. [CrossRef]
98. Xu, Q.; Zhang, L.; Cheng, B.; Fan, J.; Yu, J. S-Scheme Heterojunction Photocatalyst. *Chem* **2020**, *6*, 1543–1559. [CrossRef]
99. Ardizzone, S.; Bianchi, C.L.; Borgese, L.; Cappelletti, G.; Locatelli, C.; Minguzzi, A.; Rondinini, S.; Vertova, A.; Ricci, P.C.; Cannas, C.; et al. Physico-chemical characterization of IrO<sub>2</sub>-SnO<sub>2</sub> sol-gel nanopowders for electrochemical applications. *J. Appl. Electrochem.* **2009**, *39*, 2093–2105. [CrossRef]
100. Wang, Z.; Lin, Z.; Shen, S.; Zhong, W.; Cao, S. Advances in designing heterojunction photocatalytic materials. *Chin. J. Catal.* **2021**, *42*, 710–730. [CrossRef]
101. Wang, H.; Zhang, L.; Chen, Z.; Hu, J.; Li, S.; Wang, Z.; Liu, J.; Wang, X. Semiconductor heterojunction photocatalysts: Design, construction, and photocatalytic performances. *Chem. Soc. Rev.* **2014**, *43*, 5234–5244. [CrossRef] [PubMed]
102. Li, X.; Yu, J.; Jaroniec, M.; Chen, X. Cocatalysts for selective photoreduction of CO<sub>2</sub> into solar fuels. *Chem. Rev.* **2019**, *119*, 3962–4179. [CrossRef] [PubMed]
103. Deng, Y.; Zhao, R. Advanced Oxidation Processes (AOPs) in Wastewater Treatment. *Curr. Pollut. Rep.* **2015**, *1*, 167–176. [CrossRef]
104. Serpone, N.; Borgarello, E.; Grätzel, M. Visible light induced generation of hydrogen from H<sub>2</sub>S in mixed semiconductor dispersions; improved efficiency through inter-particle electron transfer. *J. Chem. Soc. Chem. Commun.* **1984**, *34*, 342–344. [CrossRef]

105. Serpone, N.; Maruthamuthu, P.; Pichat, P.; Pelizzetti, E.; Hidaka, H. Exploiting the interparticle electron transfer process in the photocatalysed oxidation of phenol, 2-chlorophenol and pentachlorophenol: Chemical evidence for electron and hole transfer between coupled semiconductors. *J. Photochem. Photobiol. A Chem.* **1995**, *85*, 247–255. [[CrossRef](#)]
106. Teranishi, T.; Sakamoto, M. Charge separation in type-II semiconductor heterodimers. *J. Phys. Chem. Lett.* **2013**, *4*, 2867–2873. [[CrossRef](#)]
107. Bai, S.; Jiang, J.; Zhang, Q.; Xiong, Y. Steering charge kinetics in photocatalysis: Intersection of materials syntheses, characterization techniques and theoretical simulations. *Chem. Soc. Rev.* **2015**, *44*, 2893–2939. [[CrossRef](#)] [[PubMed](#)]
108. Wang, H.; Wang, J.; Zhang, L.; Yu, Q.; Chen, Z.; Wu, S. A New Strategy for Improving the Efficiency of Low-temperature Selective Catalytic Reduction of NO<sub>x</sub> with CH<sub>4</sub> via the Combination of Non-thermal Plasma and Ag<sub>2</sub>O/TiO<sub>2</sub> Photocatalyst. *Chem. Res. Chin. Univ.* **2019**, *35*, 1062–1069. [[CrossRef](#)]
109. Wang, X.; Liu, G.; Chen, Z.G.; Li, F.; Wang, L.; Lu, G.Q.; Cheng, H.M. Enhanced photocatalytic hydrogen evolution by prolonging the lifetime of carriers in ZnO/CdS heterostructures. *Chem. Commun.* **2009**, *23*, 3452–3454. [[CrossRef](#)]
110. Grätzel, M. Photoelectrochemical cells. *Nature* **2001**, *414*, 338–344. [[CrossRef](#)] [[PubMed](#)]
111. Balayeva, N.O.; Fleisch, M.; Bahnemann, D.W. Surface-grafted WO<sub>3</sub>/TiO<sub>2</sub> photocatalysts: Enhanced visible-light activity towards indoor air purification. *Catal. Today* **2018**, *313*, 63–71. [[CrossRef](#)]
112. Wang, Y.; Shang, X.; Shen, J.; Zhang, Z.; Wang, D.; Lin, J.; Wu, J.C.S.; Fu, X.; Wang, X.; Li, C. Direct and indirect Z-scheme heterostructure-coupled photosystem enabling cooperation of CO<sub>2</sub> reduction and H<sub>2</sub>O oxidation. *Nat. Commun.* **2020**, *11*, 3043. [[CrossRef](#)]
113. Peng, Z.; Yu, J.; Jaroniec, M. All-Solid-State Z-Scheme Photocatalytic Systems. *Adv. Mater.* **2014**, *26*, 4920–4935. [[CrossRef](#)]
114. Jiang, Z.; Cheng, B.; Zhang, Y.; Wageh, S.; Al-Ghamdi, A.A.; Yu, J.; Wang, L. S-scheme ZnO/WO<sub>3</sub> heterojunction photocatalyst for efficient H<sub>2</sub>O<sub>2</sub> production. *J. Mater. Sci. Technol.* **2022**, *124*, 193–201. [[CrossRef](#)]
115. Wang, Z.; Chen, Y.; Zhang, L.; Cheng, B.; Yu, J.; Fan, J. Step-scheme CdS/TiO<sub>2</sub> nanocomposite hollow microsphere with enhanced photocatalytic CO<sub>2</sub> reduction activity. *J. Mater. Sci. Technol.* **2020**, *56*, 143–150. [[CrossRef](#)]
116. Suárez-Méndez, A.; López-Curiel, J.C.; Fuentes, G.A.; Serrano-Rosales, B.; Morales-Zárate, E.; Rivera, V.M. Thiophene-Based Oligomers Formed in-situ: A Novel Sensitizer Material of TiO<sub>2</sub>/HY Hybrid Material. *Top. Catal.* **2022**, *65*, 1218–1224. [[CrossRef](#)]
117. Zhong, Y.H.; Lei, Y.; Huang, J.F.; Xiao, L.M.; Chen, X.L.; Luo, T.; Qin, S.; Guo, J.; Liu, J.M. Design of an alkaline pyridyl acceptor-based calix [4] arene dye and synthesis of stable calixarene-TiO<sub>2</sub> porous hybrid materials for efficient photocatalysis. *J. Mater. Chem. A* **2020**, *8*, 8883–8891. [[CrossRef](#)]
118. Palmas, S.; Da Pozzo, A.; Mascia, M.; Vacca, A.; Ricci, P.C. Sensitization of TiO<sub>2</sub> nanostructures with Coumarin 343. *Chem. Eng. J.* **2012**, *211–212*, 285–292. [[CrossRef](#)]
119. Ricci, P.C.; Da Pozzo, A.; Palmas, S.; Muscas, F.; Carbonaro, C.M. Efficient charge transfer process in Coumarin 153-nanotubular TiO<sub>2</sub> hybrid system. *Chem. Phys. Lett.* **2012**, *531*, 160–163. [[CrossRef](#)]
120. Yan, S.C.; Li, Z.S.; Zou, Z.G. Photodegradation Performance of g-C<sub>3</sub>N<sub>4</sub> Fabricated by Directly Heating Melamine. *Langmuir* **2009**, *25*, 11269–11273. [[CrossRef](#)]
121. Stagi, L.; Chiriu, D.; Carbonaro, C.M.; Corpino, R.; Ricci, P.C. Structural and optical properties of carbon nitride polymorphs. *Diam. Relat. Mater.* **2016**, *68*, 84–92. [[CrossRef](#)]
122. Bledowski, M.; Wang, L.; Ramakrishnan, A.; Khavryuchenko, O.V.; Khavryuchenko, V.D.; Ricci, P.C.; Strunk, J.; Cremer, T.; Kolbeck, C.; Beranek, R. Visible-light photocurrent response of TiO<sub>2</sub>-polyheptazine hybrids: Evidence for interfacial charge-transfer absorption. *Phys. Chem. Chem. Phys.* **2011**, *13*, 21511. [[CrossRef](#)] [[PubMed](#)]
123. Ma, L.; Wang, G.; Jiang, C.; Bao, H.; Xu, Q. Synthesis of core-shell TiO<sub>2</sub>@g-C<sub>3</sub>N<sub>4</sub> hollow microspheres for efficient photocatalytic degradation of rhodamine B under visible light. *Appl. Surf. Sci.* **2018**, *430*, 263–272. [[CrossRef](#)]
124. Ni, S.; Fu, Z.; Li, L.; Ma, M.; Liu, Y. Step-scheme heterojunction g-C<sub>3</sub>N<sub>4</sub>/TiO<sub>2</sub> for efficient photocatalytic degradation of tetracycline hydrochloride under UV light. *Colloids Surf. A Physicochem. Eng. Asp.* **2022**, *649*, 129475. [[CrossRef](#)]
125. Dong, S.; Chen, S.; He, F.; Li, J.; Li, H.; Xu, K. Construction of a novel N-doped oxygen vacancy-rich TiO<sub>2</sub>N-TiO<sub>2</sub>-X/g-C<sub>3</sub>N<sub>4</sub> S-scheme heterostructure for visible light driven photocatalytic degradation of 2,4-dinitrophenylhydrazine. *J. Alloys Compd.* **2022**, *908*, 164586. [[CrossRef](#)]
126. Rodrigues, K.F.; de Moraes, N.P.; dos Santos, A.S.; Larissa, T.; Rodrigues, A.; Brunelli, D.D. Enhanced 4-chlorophenol Degradation under Visible and Solar Radiation through TiO<sub>2</sub>/g-C<sub>3</sub>N<sub>4</sub> Z-Scheme Heterojunction. *Biointerface Res. Appl. Chem.* **2022**, *13*, 113394. [[CrossRef](#)]
127. Liu, Y.; Ren, M.; Zhang, X.; Yang, G.; Qin, L.; Meng, J.; Guo, Y. Supramolecule self-assembly approach to direct Z-scheme TiO<sub>2</sub>/g-C<sub>3</sub>N<sub>4</sub> heterojunctions for efficient photocatalytic degradation of emerging phenolic pollutants. *Appl. Surf. Sci.* **2022**, *593*, 153401. [[CrossRef](#)]
128. Fu, J.; Xu, Q.; Low, J.; Jiang, C.; Yu, J. Ultrathin 2D/2D WO<sub>3</sub>/g-C<sub>3</sub>N<sub>4</sub> step-scheme H<sub>2</sub>-production photocatalyst. *Appl. Catal. B Environ.* **2019**, *243*, 556–565. [[CrossRef](#)]
129. Xia, P.; Cao, S.; Zhu, B.; Liu, M.; Shi, M.; Yu, J.; Zhang, Y. Designing a 0D/2D S-Scheme Heterojunction over Polymeric Carbon Nitride for Visible-Light Photocatalytic Inactivation of Bacteria. *Angew. Chem.-Int. Ed.* **2020**, *59*, 5218–5225. [[CrossRef](#)]
130. Xu, X.; Zhang, J.; Wang, S.; Yao, Z.; Wu, H.; Shi, L.; Yin, Y.; Wang, S.; Sun, H. Photocatalytic reforming of biomass for hydrogen production over ZnS nanoparticles modified carbon nitride nanosheets. *J. Colloid Interface Sci.* **2019**, *555*, 22–30. [[CrossRef](#)]

131. Yin, H.; Liu, J.; Shi, H.L.; Sun, L.; Yuan, X.; Xia, D. Highly efficient catalytic ozonation for oxalic acid mineralization with Ag<sub>2</sub>CO<sub>3</sub> modified g-C<sub>3</sub>N<sub>4</sub>: Performance and mechanism. *Process Saf. Environ. Prot.* **2022**, *162*, 944–954. [[CrossRef](#)]
132. Pan, S.; Jia, B.; Fu, Y. Ag<sub>2</sub>CO<sub>3</sub> nanoparticles decorated g-C<sub>3</sub>N<sub>4</sub> as a high-efficiency catalyst for photocatalytic degradation of organic contaminants. *J. Mater. Sci. Mater. Electron.* **2021**, *32*, 14464–14476. [[CrossRef](#)]
133. Jin, C.; Li, W.; Chen, Y.; Li, R.; Huo, J.; He, Q.; Wang, Y. Efficient Photocatalytic Degradation and Adsorption of Tetracycline over Type-II Heterojunctions Consisting of ZnO Nanorods and K-Doped Exfoliated g-C<sub>3</sub>N<sub>4</sub> Nanosheets. *Ind. Eng. Chem. Res.* **2020**, *59*, 2860–2873. [[CrossRef](#)]
134. Xie, K.; Wang, Y.; Zhang, K.; Zhao, R.; Chai, Z.; Du, J.; Li, J. Controllable band structure of ZnO/g-C<sub>3</sub>N<sub>4</sub> aggregation to enhance gas sensing for the dimethylamine detection. *Sens. Actuators Rep.* **2022**, *4*, 100084. [[CrossRef](#)]
135. Ding, F.; Ming, T.; Zhang, H.; Gao, Y.; Dragutan, V.; Sun, Y.; Dragutan, I.; Xu, Z. Plasmonic Ag nanoparticles decorated g-C<sub>3</sub>N<sub>4</sub> for enhanced visible-light driven photocatalytic degradation and H<sub>2</sub> production. *Resour. Chem. Mater.* **2022**, *1*, 1–7. [[CrossRef](#)]
136. Wang, H.; Sun, T.; Chang, L.; Nie, P.; Zhang, X.; Zhao, C.; Xue, X. The g-C<sub>3</sub>N<sub>4</sub> nanosheets decorated by plasmonic Au nanoparticles: A heterogeneous electrocatalyst for oxygen evolution reaction enhanced by sunlight illumination. *Electrochim. Acta* **2019**, *303*, 110–117. [[CrossRef](#)]
137. Zhang, G.; Lan, Z.A.; Lin, L.; Lin, S.; Wang, X. Overall water splitting by Pt/g-C<sub>3</sub>N<sub>4</sub> photocatalysts without using sacrificial agents. *Chem. Sci.* **2016**, *7*, 3062–3066. [[CrossRef](#)]
138. Faisal, M.; Jalalah, M.; Harraz, F.A.; El-Toni, A.M.; Khan, A.; Al-Assiri, M.S. Au nanoparticles-doped g-C<sub>3</sub>N<sub>4</sub> nanocomposites for enhanced photocatalytic performance under visible light illumination. *Ceram. Int.* **2020**, *46*, 22090–22101. [[CrossRef](#)]
139. Che, Y.; Liu, Q.; Lu, B.; Zhai, J.; Wang, K.; Liu, Z. Plasmonic ternary hybrid photocatalyst based on polymeric g-C<sub>3</sub>N<sub>4</sub> towards visible light hydrogen generation. *Sci. Rep.* **2020**, *10*, 721. [[CrossRef](#)]
140. Li, J.; Zhu, X.; Qiu, F.; Zhang, T.; Hu, F.; Peng, X. Facile preparation of Ag/Ag<sub>2</sub>WO<sub>4</sub>/g-C<sub>3</sub>N<sub>4</sub> ternary plasmonic photocatalyst and its visible-light photocatalytic activity. *Appl. Organomet. Chem.* **2019**, *33*, e4683. [[CrossRef](#)]
141. Das, S.; Deka, T.; Ningthoukhangjam, P.; Chowdhury, A. Applied Surface Science Advances A critical review on prospects and challenges of metal-oxide embedded g-C<sub>3</sub>N<sub>4</sub>-based direct Z-scheme photocatalysts for water splitting and environmental remediation. *Appl. Surf. Sci. Adv.* **2022**, *11*, 100273. [[CrossRef](#)]
142. Vasilchenko, D.; Zhurenok, A.; Saraev, A.; Gerasimov, E.; Cherepanova, S.; Kovtunova, L.; Tkachev, S.; Kozlova, E. Platinum deposition onto g-C<sub>3</sub>N<sub>4</sub> with using of labile nitratocomplex for generation of the highly active hydrogen evolution photocatalysts. *Int. J. Hydrogen Energy* **2022**, *47*, 11326–11340. [[CrossRef](#)]
143. Liu, R.; Yang, W.; He, G.; Zheng, W.; Li, M.; Tao, W.; Tian, M. Ag-Modified g-C<sub>3</sub>N<sub>4</sub> Prepared by a One-Step Calcination Method for Enhanced Catalytic Efficiency and Stability. *ACS Omega* **2020**, *5*, 19615–19624. [[CrossRef](#)] [[PubMed](#)]
144. Zeng, J.; Song, T.; Lv, M.; Wang, T.; Qin, J.; Zeng, H. Plasmonic photocatalyst Au/g-C<sub>3</sub>N<sub>4</sub>/NiFe<sub>2</sub>O<sub>4</sub> nanocomposites for enhanced visible-light-driven photocatalytic hydrogen evolution. *RSC Adv.* **2016**, *6*, 54964–54975. [[CrossRef](#)]
145. Bedia, J.; Muelas-Ramos, V.; Peñas-Garzón, M.; Gómez-Avilés, A.; Rodríguez, J.J.; Bolver, C. A review on the synthesis and characterization of metal organic frameworks for photocatalytic water purification. *Catalysts* **2019**, *9*, 52. [[CrossRef](#)]
146. Qian, Y.; Ma, D.; Zhong, J. Metal-Organic Frameworks With Variable Valence Metal-Photoactive Components: Emerging Platform for Volatile Organic Compounds Photocatalytic Degradation. *Front. Chem.* **2021**, *9*, 749839. [[CrossRef](#)] [[PubMed](#)]
147. Zhang, H.; Zhai, G.; Lei, L.; Zhang, C.; Liu, Y.; Wang, Z.; Cheng, H.; Zheng, Z.; Wang, P.; Dai, Y.; et al. Photo-induced photo-thermal synergy effect leading to efficient CO<sub>2</sub> cycloaddition with epoxide over a Fe-based metal organic framework. *J. Colloid Interface Sci.* **2022**, *625*, 33–40. [[CrossRef](#)]
148. Fu, Y.; Sun, D.; Chen, Y.; Huang, R.; Ding, Z.; Fu, X.; Li, Z. An amine-functionalized titanium metal-organic framework photocatalyst with visible-light-induced activity for CO<sub>2</sub> reduction. *Angew. Chem.-Int. Ed.* **2012**, *51*, 3364–3367. [[CrossRef](#)]
149. Hendon, C.H.; Tiana, D.; Fontecave, M.; Sanchez, C.; D'Arras, L.; Sassoie, C.; Rozes, L.; Mellot-Draznieks, C.; Walsh, A. Engineering the optical response of the titanium-MIL-125 metal-organic framework through ligand functionalization. *J. Am. Chem. Soc.* **2013**, *135*, 10942–10945. [[CrossRef](#)]
150. Han, W.; Shao, L.-H.; Sun, X.-J.; Liu, Y.-H.; Zhang, F.-M.; Yang, Y.; Dong, P.; Zhang, G. Constructing Cu Ion Sites in Mof/Cof Heterostructure for Noble-Metal-Free Photoredox Catalysis. *SSRN Electron. J.* **2022**, *317*, 121710. [[CrossRef](#)]
151. Shi, L.; Yang, L.; Zhang, H.; Chang, K.; Zhao, G.; Kako, T.; Ye, J. Implantation of Iron(III) in porphyrinic metal organic frameworks for highly improved photocatalytic performance. *Appl. Catal. B Environ.* **2018**, *224*, 60–68. [[CrossRef](#)]
152. Lou, W.; Wang, L.; Dong, S.; Cao, Z.; Sun, J.; Zhang, Y. A facility synthesis of bismuth-iron bimetal MOF composite silver vanadate applied to visible light photocatalysis. *Opt. Mater.* **2022**, *126*, 112168. [[CrossRef](#)]
153. Li, Q.; Fan, Z.; Zhang, L.; Li, Y.; Chen, C.; Zhao, R.; Zhu, W. Boosting and tuning the visible photocatalytic degradation performances towards reactive blue 21 via dyes@MOF composites. *J. Solid State Chem.* **2019**, *269*, 465–475. [[CrossRef](#)]
154. Wang, Q.; Gao, Q.; Al-Enizi, A.M.; Nafady, A.; Ma, S. Recent advances in MOF-based photocatalysis: Environmental remediation under visible light. *Inorg. Chem. Front.* **2020**, *7*, 300–339. [[CrossRef](#)]
155. Doustkhah, E.; Esmat, M.; Fukata, N.; Ide, Y.; Hanaor, D.A.H.; Assadi, M.H.N. MOF-derived nanocrystalline ZnO with controlled orientation and photocatalytic activity. *Chemosphere* **2022**, *303*, 134932. [[CrossRef](#)] [[PubMed](#)]
156. Zeng, T.; Shi, D.; Cheng, Q.; Liao, G.; Zhou, H.; Pan, Z. Construction of novel phosphonate-based MOF/P-TiO<sub>2</sub> heterojunction photocatalysts: Enhanced photocatalytic performance and mechanistic insight. *Environ. Sci. Nano* **2020**, *7*, 861–879. [[CrossRef](#)]

157. Wei, Z.; Zhu, Y.; Guo, W.; Liu, J.; Jiang, Z.; Shangguan, W. Enhanced photocatalytic overall water splitting via MOF-derived tetragonal BiVO<sub>4</sub>-based solid solution. *Chem. Eng. J.* **2021**, *414*, 128911. [CrossRef]
158. Jing, C.; Zhang, Y.; Zheng, J.; Ge, S.; Lin, J.; Pan, D.; Naik, N.; Guo, Z. In-situ constructing visible light CdS/Cd-MOF photocatalyst with enhanced photodegradation of methylene blue. *Particuology* **2022**, *69*, 111–122. [CrossRef]
159. Karimia, M.; Sadeghia, S.; Gavinehroudi, R.G.; Mohebal, H.; Mahjoub, A.; Heydari, A. g-C<sub>3</sub>N<sub>4</sub>@Ce-MOF Z-scheme heterojunction photocatalyzed cascade aerobic oxidative functionalization of styrene. *New J. Chem.* **2021**, *45*, 6671–6681. [CrossRef]
160. Wu, H.; Sun, Q.; Chen, J.; Wang, G.Y.; Wang, D.; Zeng, X.F.; Wang, J.X. Citric acid-assisted ultrasmall CeO<sub>2</sub> nanoparticles for efficient photocatalytic degradation of glyphosate. *Chem. Eng. J.* **2021**, *425*, 130640. [CrossRef]
161. Han, J.; Deng, Y.; Li, N.; Chen, D.; Xu, Q.; Li, H.; He, J.; Lu, J. A  $\pi$ - $\pi$  stacking perylene imide/Bi<sub>2</sub>WO<sub>6</sub> hybrid with dual transfer approach for enhanced photocatalytic degradation. *J. Colloid Interface Sci.* **2021**, *582*, 1021–1032. [CrossRef]
162. Cai, T.; Zeng, W.; Liu, Y.; Wang, L.; Dong, W.; Chen, H.; Xia, X. A promising inorganic-organic Z-scheme photocatalyst Ag<sub>3</sub>PO<sub>4</sub>/PDI supermolecule with enhanced photoactivity and photostability for environmental remediation. *Appl. Catal. B Environ.* **2020**, *263*, 118327. [CrossRef]
163. Zeng, W.; Cai, T.; Liu, Y.; Wang, L.; Dong, W.; Chen, H.; Xia, X. An artificial organic-inorganic Z-scheme photocatalyst WO<sub>3</sub>@Cu@PDI supramolecular with excellent visible light absorption and photocatalytic activity. *Chem. Eng. J.* **2020**, *381*, 122691. [CrossRef]
164. Shirmardi, A.; Teridi, M.A.M.; Azimi, H.R.; Basirun, W.J.; Jamali-Sheini, F.; Yousefi, R. Enhanced photocatalytic performance of ZnSe/PANI nanocomposites for degradation of organic and inorganic pollutants. *Appl. Surf. Sci.* **2018**, *462*, 730–738. [CrossRef]
165. Sutar, R.S.; Barkul, R.P.; Delekar, S.D.; Patil, M.K. Sunlight assisted photocatalytic degradation of organic pollutants using g-C<sub>3</sub>N<sub>4</sub>-TiO<sub>2</sub> nanocomposites. *Arab. J. Chem.* **2020**, *13*, 4966–4977. [CrossRef]
166. Porcu, S.; Castellino, M.; Roppolo, I.; Carbonaro, C.M.; Palmas, S.; Mais, L.; Casula, M.F.; Neretina, S.; Hughes, R.A.; Secci, F.; et al. Highly efficient visible light phenyl modified carbon nitride/TiO<sub>2</sub> photocatalyst for environmental applications. *Appl. Surf. Sci.* **2020**, *531*, 147394. [CrossRef]
167. Wang, J.; Wang, G.; Cheng, B.; Yu, J.; Fan, J. Congo Red photodegradation. *Chin. J. Catal.* **2021**, *42*, 56–68. [CrossRef]
168. Hamdy, M.S.; Abd-Rabboh, H.S.M.; Benaissa, M.; Al-Metwaly, M.G.; Galal, A.H.; Ahmed, M.A. Fabrication of novel polyaniline/ZnO heterojunction for exceptional photocatalytic hydrogen production and degradation of fluorescein dye through direct Z-scheme mechanism. *Opt. Mater.* **2021**, *117*, 111198. [CrossRef]
169. Liang, Q.; Cui, S.; Liu, C.; Xu, S.; Yao, C.; Li, Z. Self-assembly of triptycene-based polymer on cadmium sulfide nanorod to construct core-shell nanostructure for efficient visible-light-driven photocatalytic H<sub>2</sub> evolution. *Chem. Eng. J.* **2019**, *364*, 102–110. [CrossRef]
170. Zang, S.; Zhang, G.; Lan, Z.A.; Zheng, D.; Wang, X. Enhancement of photocatalytic H<sub>2</sub> evolution on pyrene-based polymer promoted by MoS<sub>2</sub> and visible light. *Appl. Catal. B Environ.* **2019**, *251*, 102–111. [CrossRef]
171. Zhu, Y.P.; Yin, J.; Abou-Hamad, E.; Liu, X.; Chen, W.; Yao, T.; Mohammed, O.F.; Alshareef, H.N. Highly Stable Phosphonate-Based MOFs with Engineered Bandgaps for Efficient Photocatalytic Hydrogen Production. *Adv. Mater.* **2020**, *32*, e1906368. [CrossRef]
172. Hieu, V.Q.; Lam, T.C.; Khan, A.; Thi Vo, T.T.; Nguyen, T.Q.; Doan, V.D.; Tran, D.L.; Le, V.T.; Tran, V.A. TiO<sub>2</sub>/Ti<sub>3</sub>C<sub>2</sub>/g-C<sub>3</sub>N<sub>4</sub> ternary heterojunction for photocatalytic hydrogen evolution. *Chemosphere* **2021**, *285*, 131429. [CrossRef]
173. Gong, S.; Teng, X.; Niu, Y.; Liu, X.; Xu, M.; Xu, C.; Ji, L.; Chen, Z. Construction of S-scheme 0D/2D heterostructures for enhanced visible-light-driven CO<sub>2</sub> reduction. *Appl. Catal. B Environ.* **2021**, *298*, 120521. [CrossRef]
174. Yang, C.; Wang, Y.; Yu, J.; Cao, S. Ultrathin 2D/2D Graphdiyne/Bi<sub>2</sub>WO<sub>6</sub> Heterojunction for Gas-Phase CO<sub>2</sub> Photoreduction. *ACS Appl. Energy Mater.* **2021**, *4*, 8734–8738. [CrossRef]
175. Kong, X.J.; He, T.; Zhou, J.; Zhao, C.; Li, T.C.; Wu, X.Q.; Wang, K.; Li, J.R. In Situ Porphyrin Substitution in a Zr(IV)-MOF for Stability Enhancement and Photocatalytic CO<sub>2</sub> Reduction. *Small* **2021**, *17*, 2005357. [CrossRef]
176. Ke, X.; Zhang, J.; Dai, K.; Fan, K.; Liang, C. Integrated S-Scheme Heterojunction of Amine-Functionalized 1D CdSe Nanorods Anchoring on Ultrathin 2D SnNb<sub>2</sub>O<sub>6</sub> Nanosheets for Robust Solar-Driven CO<sub>2</sub> Conversion. *Sol. RRL* **2021**, *5*, 2000805. [CrossRef]
177. Wang, H.; Li, H.; Chen, Z.; Li, J.; Li, X.; Huo, P.; Wang, Q. TiO<sub>2</sub> modified g-C<sub>3</sub>N<sub>4</sub> with enhanced photocatalytic CO<sub>2</sub> reduction performance. *Solid State Sci.* **2020**, *100*, 106099. [CrossRef]
178. Yang, H.; He, D.; Liu, C.; Zhang, T.; Qu, J.; Jin, D.; Zhang, K.; Lv, Y.; Zhang, Z.; Zhang, Y. Visible-light-driven photocatalytic disinfection by S-scheme  $\alpha$ -Fe<sub>2</sub>O<sub>3</sub>/g-C<sub>3</sub>N<sub>4</sub> heterojunction: Bactericidal performance and mechanism insight. *Chemosphere* **2022**, *287*, 132072. [CrossRef] [PubMed]
179. Zhang, X.; Tian, F.; Lan, X.; Liu, Y.; Yang, W.; Zhang, J.; Yu, Y. Building P-doped MoS<sub>2</sub>/g-C<sub>3</sub>N<sub>4</sub> layered heterojunction with a dual-internal electric field for efficient photocatalytic sterilization. *Chem. Eng. J.* **2022**, *429*, 132588. [CrossRef]
180. Yang, R.; Song, G.; Wang, L.; Yang, Z.; Zhang, J.; Zhang, X.; Wang, S.; Ding, L.; Ren, N.; Wang, A.; et al. Full Solar-Spectrum-Driven Antibacterial Therapy over Hierarchical Sn<sub>3</sub>O<sub>4</sub>/PDINH with Enhanced Photocatalytic Activity. *Small* **2021**, *17*, 2102744. [CrossRef]
181. Rathna, T.; PonnarEttiyappan, J.B.; RubenSudhakar, D. Fabrication of visible-light assisted TiO<sub>2</sub>-WO<sub>3</sub>-PANI membrane for effective reduction of chromium (VI) in photocatalytic membrane reactor. *Environ. Technol. Innov.* **2021**, *24*, 102023. [CrossRef]

182. Shen, H.; Shao, Z.; Zhao, Q.; Jin, M.; Shen, C.; Deng, M.; Zhong, G.; Huang, F.; Zhu, H.; Chen, F.; et al. Facile synthesis of novel three-dimensional Bi<sub>2</sub>S<sub>3</sub> nanocrystals capped by polyvinyl pyrrolidone to enhance photocatalytic properties under visible light. *J. Colloid Interface Sci.* **2020**, *573*, 115–122. [[CrossRef](#)]
183. Yang, R.; Zhong, S.; Zhang, L.; Liu, B. PW12/CN@Bi<sub>2</sub>WO<sub>6</sub> composite photocatalyst prepared based on organic-inorganic hybrid system for removing pollutants in water. *Sep. Purif. Technol.* **2020**, *235*, 116270. [[CrossRef](#)]